Multiblock parallel high-order implicit residual smoothing time scheme for compressible Navier–Stokes equations

Bienner, A.; Gloerfelt, X.; Yalçın, Özgür; Cinnella, P.

DOI
10.1016/j.compfluid.2023.106138

Publication date
2024

Document Version
Final published version

Published in
Computers and Fluids

Citation (APA)
Bienner, A., Gloerfelt, X., Yalçın, Ö., & Cinnella, P. (2024). Multiblock parallel high-order implicit residual smoothing time scheme for compressible Navier–Stokes equations. *Computers and Fluids*, *269*, Article 106138. https://doi.org/10.1016/j.compfluid.2023.106138

Computers and Fluids 269 (2024) 106138

Contents lists available at ScienceDirect

Computers and Fluids

journal homepage: www.elsevier.com/locate/compfluid

Multiblock parallel high-order implicit residual smoothing time scheme for compressible Navier–Stokes equations

A. Bienner [a], X. Gloerfelt [a,*], Ö. Yalçın [a], P. Cinnella [b]

[a] DynFluid Laboratory, Arts et Métiers Institute of Technology, 151 bd. de l'Hôpital, Paris, 75013, France
[b] Jean Le Rond D'Alembert Institute, Sorbonne University, 4 place Jussieu, Paris, 75005, France

ARTICLE INFO

Keywords:
High-order numerical algorithms
Implicit time advancement
Residual smoothing
Multi-block curvilinear domains
High-fidelity parallel computation

ABSTRACT

In direct and large eddy simulations, very small space steps are used close to the solid walls in order to resolve the boundary-layer structures. Due to the restrictive CFL stability criteria of explicit time-stepping schemes, the maximum allowable time step is also very small, leading to high computational costs, notably for converging flow statistics. The use of an implicit integration scheme may overcome this limitation at the price of an increased computational cost per step. Moreover, the most commonly used fully implicit schemes induce higher errors due to the necessary approximations and poor dispersion and dissipation properties. As a compromise, a fourth-order implicit residual smoothing scheme (IRS4), successfully validated for a finite volume solver in Cinnella nad Content (2016); Hoarau and Cinnella (2020), has been introduced in a multiblock high-order finite-difference solver. Several improvements are proposed to ensure better dissipation properties, a more efficient treatment of physical boundaries and an accurate and stable parallel multiblock implementation. For moderate CFL numbers, a similar accuracy as the explicit method is obtained with substantial savings in terms of computational time.

1. Introduction

High-order numerical methods are becoming the golden rule for direct numerical simulations (DNS) and large-eddy simulations (LES) of turbulent flows and aeroacoustics. In order to maintain numerical accuracy and due to the time scales comparable to the spatial scales, the Courant–Friedrichs–Lewy (CFL) number is close to unity. and generally explicit time integration schemes, such as Runge–Kutta or Adams–Bashforth schemes, are used. The limit is then dictated by the physics rather than the numerical stability. However, in the presence of solid boundaries, thin turbulent boundary layers develop along the walls, requiring the use of very small mesh sizes. In such a situation, stability constraints of explicit schemes impose time steps much smaller than the characteristic time of viscosity-dominated turbulent structures near the wall, despite the physics would allow CFL of the order of 10 [1]. In the incompressible regime, when the stability limit is dictated by the viscous criterion, an implicit scheme can remove the limit at the price of the solution of a linear system. The cost being moderate the algorithm remains efficient. For the compressible Navier–Stokes equations the implicit treatment of the convective fluxes necessitates the solution of nonlinear systems. If a high-accurate time integration is chosen, such as implicit Runge–Kutta schemes or linear multistep methods (Adams–Moulton or Backward Differentiation Formula schemes), the overhead may outweigh the benefits of increasing the time step beyond the CFL limit.

One way to relax the severe stability limitations of explicit schemes without going to the trouble of fully implicit ones, is the use of residual smoothing techniques. These consist in running the simulations with a CFL number higher than the maximum value allowed by the explicit scheme in use, and redistributing errors in the residuals over neighboring cells by applying an explicit or implicit smoothing operator. Explicit residual smoothing, discussed in [2,3] in the case of second-order accurate smoothing operators, does not allow significant increases in CFL, limiting the potential gains over an unsmoothed explicit scheme. Implicit Residual Smoothing (IRS), a technique originally introduced to speed-up convergence to steady-state solutions, can be extended to high order [4,5] and can accurately simulate unsteady flow at CFL between 5 and 10 at a moderate overhead. IRS may be one order of magnitude cheaper than a fully implicit method where the nonlinear system is solved to strict tolerance. In the context of compressible flow simulations, IRS was introduced at a time when computing power essentially only allowed the calculation of steady-state solutions. A relatively accurate (second-order) implicit phase was constructed by Lerat and coworkers [6–9] by simplifying a Lax–Wendroff-type implicit scheme. Based on second-order central differencing, it acts as a

* Corresponding author.
E-mail address: xavier.gloerfelt@ensam.eu (X. Gloerfelt).

https://doi.org/10.1016/j.compfluid.2023.106138
Received 23 May 2023; Received in revised form 16 October 2023; Accepted 23 November 2023
Available online 1 December 2023

Laplacian smoother to accelerate convergence. The implicit phase of Lerat et al. bears a strong resemblance to the implicit phase introduced later by Jameson and coworkers [2,10] to smooth/filter the solution. A fully implicit version using the approximate Jacobian of the residual instead of a scalar smoothing coefficient was proposed in [11] in the context of multigrid acceleration for steady solutions of Navier–Stokes equations, and requires the inversion of a block matrix using approximate splitting. IRS was used in several computational fluid dynamics (CFD) codes to speed-up convergence of steady Euler and Navier–Stokes calculations in conjunction with multigrid algorithms [12–16]. A fourth-order accurate version was introduced in [4] and applied to the LES and DNS of selected geometrically simple flow configurations. A finite-volume multi-domain formulation was discussed in [5] and shown to be efficient for LES in turbomachinery in conjunction with a third-order accurate spatial scheme. The fourth-order IRS relies on a bi-Laplacian filter to damp high-frequency modes of the residual, which leads to the solution of pentadiagonal systems for each space direction and Runge–Kutta stage. Thanks to the efficient inversion of scalar pentadiagonal matrices, the extra computational cost associated with the implicit operator was shown to remain much lower than standard implicit schemes at least for the considered configurations. As discussed in the paper, a multi-domain implementation can require simplifications of the implicit matrix that may hinder robustness. Furthermore, the numerical dissipation properties of the implicit scheme are also modified and may lead to reduced numerical stability in conjunction with higher-order schemes, such as the tenth-order-accurate scheme considered in this study. Recently, a methodology for enlarging the stability of RK schemes by preconditioning the residuals at each RK step [17,18], called TASE (time-accurate highly stable explicit) has been introduced in the context of stiff ordinary differential equations, which bears similarities with the IRS approach. However, TASE requires the computation and inversion of an exact or approximate Jacobian of the explicit residual, which may be not straightforward for unsteady problems and high-order schemes.

The objective of the present work is manyfold: (i) first, the IRS is extended to a curvilinear finite-difference formulation, more suitable than the finite-volume formulation to achieve very high-order spatial accuracy; (ii) a detailed study of the numerical dissipation is carried out, and a selective filtering strategy on the solution variables is introduced to ensure the correct damping of small scales at high CFL numbers; (iii) finally, the numerical properties of boundary and interface treatment, which are critical for DNS and LES on massively parallel computers, are presented.

The paper is organized as follows: Section 2 presents the time and space discretization schemes at stake. Section 3 gives the principles and numerical properties of the IRS implicit phase, notably in the Fourier space and illustrates its implementation in a finite-difference code with curvilinear transforms. The problem of boundary and interface treatments is addressed in Section 4. Section 5 gives some numerical applications showing the efficiency and the benefits of the current time implicit strategy for a set of flow problems of increasing complexity.

2. Baseline numerical methods

2.1. Space discretization schemes

We consider a system of conservation laws of the form

$$\frac{\partial w}{\partial t} + \sum_d \frac{\partial f_d(w)}{\partial x_d} = 0 \tag{1}$$

where d is the number of space dimensions, f_d is the flux function in the dth direction, and x_d the corresponding space coordinate. The semi-discrete form of (1) is written as

$$w_t + \mathcal{R}(w) = 0\,, \tag{2}$$

$\mathcal{R}$ being the space approximation operator. In the present work, since we are mostly interested in developing an efficient and accurate time integration scheme, we have chosen a spatial discretization of much higher accuracy than the time discretization under consideration. Specifically, we adopt a tenth-order central finite-difference scheme. For a 1D problem on a uniform mesh of size Δx, $x_j = j\Delta x$ and the semi-discrete scheme in space reads:

$$\left(w_t\right)_j + \frac{(\delta \mathcal{F})_j}{\Delta x} = 0$$

where δ is the classical difference operator over one cell:

$$\delta(\bullet)_{j+\frac{1}{2}} = (\bullet)_{j+1} - (\bullet)_j \tag{3}$$

and the numerical flux $\mathcal{F}_{j+\frac{1}{2}}$ at cell interface $j+\frac{1}{2}$ is

$$\mathcal{F}_{j+\frac{1}{2}} = \left[\left(I - \frac{1}{6}\delta^2 + \frac{1}{30}\delta^4 - \frac{1}{140}\delta^6 + \frac{1}{1260}\delta^8\right)\mu f\right]_{j+\frac{1}{2}} \tag{4}$$

where f is the physical flux, and μ is the cell average operator $\mu(\bullet)_{j+\frac{1}{2}} = \frac{1}{2}\left((\bullet)_{j+1} + (\bullet)_j\right)$. Central difference methods are zero dissipative and prone to aliasing errors. Even starting with a smooth solution, nonlinearity can excite odd-even decoupling, and dissipation or filtering is needed to remove grid-to-grid oscillations. The latter are preferentially generated near the approximate physical boundary conditions and can arise due to the successive application of the first-order derivative operator in computing the derivatives of viscous fluxes. The problem is further complicated in the presence of sharp flow discontinuities, such as shocks, and in the context of large-eddy simulations. The unresolved modes introduce an aliasing error and have to be dissipated by adding some form of numerical dissipation or filtering. Alternative options are given by convective splitting strategies that ensure the exact conservation of physical quantities such as the kinetic energy or the entropy at the discrete level [19–22], or by considering staggered arrangements of variables [23–25]. For strategies relying on unsplitted fluxes and colocated variables, the nature, amount and form of the numerical dissipation have a strong influence on the solution accuracy [26,27]. In Ref. [4], a scalar artificial dissipation (AD) was used (we omit here the shock-capturing term for simplicity). The approximation of flux derivatives is supplemented by a ninth-order dissipation term:

$$\mathcal{F}_{j+\frac{1}{2}} = \left[\left(I - \frac{1}{6}\delta^2 + \frac{1}{30}\delta^4 - \frac{1}{140}\delta^6 + \frac{1}{1260}\delta^8\right)\mu f - \mathcal{D}^{AD}\right]_{j+\frac{1}{2}}$$

with

$$\mathcal{D}^{AD}_{j+\frac{1}{2}} = \frac{1}{1260}(\lambda^e \delta^9 w)_{j+\frac{1}{2}} \tag{5}$$

where λ^e is the spectral radius of the inviscid flux Jacobian. The coefficient $1/1260$ is used by analogy with a ninth-order MUSCL scheme [4]. As an alternative to artificial viscosity, in [26,27] we also used selective filtering (SF). A filtered quantity w_j^* is computed by using a tenth-order centered filter built on an eleven-point stencil [28,29] :

$$w_j^* = w_j - \chi \mathcal{D}_j^{SF} \quad \text{with} \quad \mathcal{D}_j^{SF} = \sum_{l=-5}^{5} d_l\, w_{j+l}\,, \tag{6}$$

with the coefficient χ ranging between 0 and 1. In most applications, a value $\chi \in [0.1\,, 0.2]$ is used, so that a minimal amount of dissipation is introduced. The filter has symmetric coefficients d_l, so that it is nondispersive. The connection with artificial dissipation has been clearly highlighted by Edoh et al. [30] (see also [31,32]), who showed that the performance of explicit AD and SF are similar. Both methods adjust the amount of dissipation to the mesh size Δx. One pitfall of the filtering approach is that it does not take into account the time step Δt, and for very small time steps (or CFL numbers), the repeated application of the filter can lead to an overdissipation. A simple trick proposed in [30] to overcome this artifact is to replace χ by

$$\min\{\chi, \mathrm{CFL}_{\mathrm{local}}\}\,, \tag{7}$$

where $\mathrm{CFL}_{\mathrm{local}}$ is based on the spectral radius of inviscid fluxes at the considered point and in the considered direction. Another possibility not explored in this work is the temporally consistent filter based on viscous scaling proposed by [33]. The filtering procedure, Eqs. (6), (7), is used in the present implementation. We will see that selective filtering independent on Δt has also some advantages in the context of IRS time advancement.

2.2. Time discretization scheme

The baseline time-stepping procedure is the explicit four-stage low-storage Runge–Kutta (RK4) of Jameson et al. [34], which may be written as:

$$\begin{cases} w^{(0)} = w^n \\ \Delta w^{(k)} = -\alpha_k \Delta t \mathcal{R}(w^{(k-1)}), \quad k = 1, \dots, s \\ w^{n+1} = w^{(s)} \end{cases} \tag{8}$$

where w^n is the numerical solution at time $n\Delta t$, $\Delta w^{(k)} = w^{(k)} - w^{(0)}$ is the solution increment at the kth RK stage, $s = 4$ is the number of stages and α_k are the scheme coefficients ($\alpha_1 = 1/4$, $\alpha_2 = 1/3$, $\alpha_3 = 1/2$, $\alpha_4 = 1$). Its order of accuracy is equal to four for linear equations and reduces down to two for nonlinear problems. When coupled with the tenth-order centered approximation, RK4 is stable under a CFL condition:

$$\mathrm{CFL} = \frac{\Delta t \lambda_e}{\Delta x} \lessapprox 1.598$$

where the spectral radius of the inviscid flux Jacobians, λ_e, is the sum of the velocity magnitude U and the sound speed c. For a viscous problem, RK4 has also to satisfy a viscous stability condition:

$$\frac{\Delta t \lambda_v}{\Delta x^2} \lessapprox 0.696$$

where λ_v is the spectral radius of viscous flux Jacobians. In practice, the time step is taken as the minimum time step given by the CFL condition and the viscous condition (also called Fourier criterion). When solving compressible Navier–Stokes equations, the CFL criterion is more restrictive due to the contribution of the sound speed to the definition of the CFL, except for very low Mach numbers and fine grids. However, using time steps larger than those allowed by the CFL condition in partially implicit time integration methods can still lead to the violation of the Fourier criterion (see discussion in Section 5.8).

3. Time integration using high-order implicit residual smoothing

3.1. Principle of implicit residual smoothing

In the original developments by Lerat and coworkers [6–9], an implicit phase was proposed for a general class of three-point schemes using an approximate Lax–Wendroff-like implicit operator. Starting from the 2D Euler equations, written as:

$$w_t + f(w)_x + g(w)_y = 0$$

and denoting $A = \partial f/\partial w$ and $B = \partial g/\partial w$ the Jacobian matrices, the complete implicit phase is:

$$\Delta w + \theta \frac{\Delta t^2}{2} \left\{ \left[A^2 (\Delta w)_x + AB(\Delta w)_y \right]_x + \left[BA(\Delta w)_x + B^2 (\Delta w)_y \right]_y \right\} = \Delta w^{expl}$$

where Δw is the solution increment and Δw^{expl} represents the explicit phase (e.g., $\Delta w^{expl} = -\frac{(\delta F)_j}{\Delta x}$ for a 1D inviscid problem). It is unconditionally stable for $\theta \leq -1/2$. A first simplification consists in the suppression of cross-derivative terms:

$$\Delta w + \theta \frac{\Delta t^2}{2} \left\{ \left[A^2 (\Delta w)_x \right]_x + \left[B^2 (\Delta w)_y \right]_y \right\} = \Delta w^{expl}$$

An approximate factorization per spatial direction is then used, yielding:

$$\begin{cases} \Delta w^* + \theta \frac{\Delta t^2}{2} \left[A^2 (\Delta w^*)_x \right]_x = \Delta w^{expl} \\ \Delta w + \theta \frac{\Delta t^2}{2} \left[B^2 (\Delta w)_y \right]_y = \Delta w^* \end{cases}$$

The preceding relations are further simplified by replacing the Jacobian matrices by their spectral radius ρ:

$$\begin{cases} \Delta w^* + \theta \frac{\Delta t^2}{2} \left[\rho(A)^2 (\Delta w^*)_x \right]_x = \Delta w^{expl} \\ \Delta w + \theta \frac{\Delta t^2}{2} \left[\rho(B)^2 (\Delta w)_y \right]_y = \Delta w^* \end{cases}$$

After discretization by second-order central differences, the implicit operator $\mathcal{J}$ for each direction reads:

$$\mathcal{J} = 1 - \theta_2 \left(\frac{\Delta t}{\Delta x} \right)^2 \delta(\lambda^{e2} \delta) \tag{9}$$

where δ is the differencing operator (3), λ^e denotes the spectral radius of the flux Jacobians in each direction and $\theta_2 \geq 0$ is the value of the coefficient for the second-order scheme. With such a scheme, a scalar tridiagonal system must be solved for each space dimension. A similar implicit operator was used by Jameson & Baker [2] to increase the CFL number of an explicit Runge–Kutta time-stepping scheme for steady problems. The so-called "implicit residual smoothing" is applied at each RK stage as:

$$\begin{cases} w^{(0)} = w^n \\ \mathcal{J} \Delta w^{(k)} = -\alpha_k \Delta t \mathcal{R}(w^{(k-1)}), \quad k = 1, \dots, s \\ w^{n+1} = w^{(s)} \end{cases} \tag{10}$$

where w^n is the solution vector at time iteration n and the implicit operator $\mathcal{J}$ of Jameson & Baker (JB) reads:

$$\mathcal{J}_{JB} = 1 - \varepsilon \left(\frac{\Delta t}{\Delta x} \right)^2 \delta^2 \quad \text{with} \quad \varepsilon \geq \frac{1}{4} \left[\left(\frac{\mathrm{CFL}}{\mathrm{CFL}^{expl}} \right)^2 - 1 \right]$$

with ε a constant parameter that depends on the maximum allowable CFL of the underlying explicit scheme and the desired CFL in the implicit procedure. Note that, in the context of steady state computations using multigrid smoothers, alternative formulations of ε as a function of the CFL have been proposed in the literature [10,35]. The $\mathcal{J}_{JB}$ operator has only first-order accuracy [36], whereas the Lax–Wendroff IRS operator (9) maintains second-order accuracy, and is then noted IRS2. The IRS2 was used in conjunction with RK time stepping by Cinnella & Lerat [37]. An extension to fourth-order (IRS4) was first proposed by Cinnella and Content [4], by keeping the same form of the operator (9) but replacing the Laplacian smoothing by a bi-Laplacian smoothing:

$$\mathcal{J} = 1 + \theta_4 \left(\frac{\Delta t}{\Delta x} \right)^4 \delta(\lambda^{e4} \delta^3), \tag{11}$$

which implies the resolution of a pentadiagonal system for each space direction. IRS4 is unconditionally stable for $\theta_4 \gtrsim 0.0023$ (see Section 4.2). We use the value $\theta_4 = 0.0025$ in the following. The additional error introduced by the IRS4 operator with respect to the explicit scheme takes the form [4]:

$$-\frac{1}{12} \theta_4 \Delta t^4 \lambda^{e4} \frac{\partial^5 f_d^e}{\partial x^5} + \mathcal{O}(\Delta t^4) \tag{12}$$

with f_d^e the inviscid flux in the considered direction d. Being proportional to an odd derivative, this error has a dispersive nature. As the RK scheme is second-order in general, the additional error coming from the IRS4 is expected to have a negligible influence on the overall accuracy of the baseline time scheme.

3.2. Interpretation in Fourier space

The main idea of IRS is to stabilize the scheme by smoothing the residuals with a Laplacian filter (IRS2) or a bi-Laplacian filter (IRS4). The IRS operator acts on the difference scheme by contracting its support and thus relaxes the restriction on the time step imposed by the CFL condition. This behavior can be easily interpreted using Fourier symbols of the operators (denoted with $\widehat{\bullet}$). Fourier analysis also provides a simple means of determining errors produced by the discretization in absence of boundary conditions.

The amplification factor of the RK4 scheme is found to be:

$$\hat{g}(\zeta) = 1 + \zeta + \zeta^2/2 + \zeta^3/6 + \zeta^4/24\,, \quad \zeta \in \mathbb{C} \tag{13}$$

The stability region can be represented in the complex plane. The black line in Fig. 1 marks the stability boundary ($|\hat{g}(\zeta)| = 1$). The gray color area denotes the unstable region ($|\hat{g}(\zeta)| > 1$). Consider the linear scalar advection problem

$$w_t + a w_x = 0 \quad (a > 0) \tag{14}$$

The locus of the FD operator (4) is given by :

$$\hat{\mathcal{R}}(k\Delta x) = \frac{2\,i\,a}{\Delta x}\sin\left(\frac{k\Delta x}{2}\right)\cos\left(\frac{k\Delta x}{2}\right)\left[1 + \frac{2}{3}\sin^3\left(\frac{k\Delta x}{2}\right) + \frac{8}{15}\sin^5\left(\frac{k\Delta x}{2}\right) + \frac{16}{35}\sin^7\left(\frac{k\Delta x}{2}\right) + \frac{128}{315}\sin^9\left(\frac{k\Delta x}{2}\right)\right] \tag{15}$$

with $i = \sqrt{-1}$ and $k\Delta x$ the reduced wavenumber. The space discretization is nondissipative and its locus lies on the imaginary axis. The Fourier symbol of the artificial dissipation operator (5) is given by:

$$\hat{D}^{AD}(k\Delta x) = \frac{a}{\Delta x}\frac{256}{315}\sin^{10}\left(\frac{k\Delta x}{2}\right) \tag{16}$$

and its locus lies on the real axis. In order for the discrete scheme to be stable, the locus of the spatial operator $(-\hat{\mathcal{R}} + \hat{D}^{AD})$ must remain within the stability region of the RK integration scheme, as shown in Fig. 1a. As the CFL increases, the locus will expand and ultimately exit the stability region, as exemplified in Fig. 1(b–f).

The IRS smoothing in Eq. (10) corresponds to a modification of the Fourier symbol of the spatial operator, which becomes $(-\hat{\mathcal{R}} + \hat{D}^{AD})/\hat{\mathcal{J}}$, where the Fourier symbol of IRS4 reads:

$$\hat{\mathcal{J}} = 1 + 16\,\theta_4 \mathrm{CFL}^4 \sin^4\left(\frac{k\Delta x}{2}\right) \tag{17}$$

The modified locii for IRS4 are plotted in Fig. 1 for CFL = 1 to 6. The IRS operator contracts the spatial locus, which is flattened on the imaginary axis due to the dispersive nature of the IRS operator. This also implies that, as the CFL increases, the dissipation error decreases and tends to zero.

3.3. Von Neumann stability

To better understand the role of the numerical dissipation in combination with IRS smoothing, a Von Neumann stability analysis is conducted. In the linear scalar case of a transport Eq. (14), the RK algorithm is developed as :

$$w_j^{n+1} = w_j^n + \sum_{s=1}^{4}\gamma_s \Delta t^s \frac{\partial^s w_j^n}{\partial t^s} + \cdots \quad \text{where} \quad \gamma_s = \prod_{q=4-s+1}^{4}\alpha_q \tag{18}$$

with w_j^n is the solution at grid index j and time iteration n. By applying a Fourier transform to (18), we write the amplification factor for the discretized equation without numerical dissipation as :

$$\hat{\mathcal{G}}^0 = \frac{\hat{w}_j^{n+1}}{\hat{w}_j^n} = 1 - \sum_{s=1}^{4}\gamma_s \sigma^s \hat{\mathcal{R}}^s \tag{19}$$

where $\sigma = a\Delta t/\Delta x$ is the CFL number. Introducing artificial dissipation, the amplification factor becomes:

$$\hat{\mathcal{G}}^{AD} = 1 - \sum_{s=1}^{4}\gamma_s \sigma^s \left(\hat{\mathcal{R}} - \hat{D}^{AD}\right)^s \tag{20}$$

On the other hand, the filtering operation (6), applied at the last RK stage, corresponds to a convolution operation in physical space, so that the amplification factor after filtering is multiplied by $1 - \chi\hat{D}^{SF}$:

$$\hat{\mathcal{G}}^{SF} = \left(1 - \sum_{s=1}^{4}\gamma_s \sigma^s \hat{\mathcal{R}}^s\right)\left(1 - \hat{D}^{SF}\right) \tag{21}$$

where the Fourier symbol of SF is obtained by applying a Fourier transform to (6) :

$$\hat{D}^{SF}(k\Delta x) = \chi\left(d_0 + \sum_{l=1}^{5} 2 d_l \cos(l k\Delta x)\right) = \chi \sin^{10}\left(\frac{k\Delta x}{2}\right) \tag{22}$$

Note that, for $a/\Delta x = 1$, the Fourier symbol of the tenth-order filter is the same as the one of the ninth-order artificial dissipation when chosing $\chi = 256/315$. The role of the numerical dissipation is displayed in Fig. 2 for CFL numbers between 1 and 15. We first focus on the base scheme without stabilization in Fig. 2(a). For the selected value of the IRS4 coefficient ($\theta_4 = 0.0025$), it is apparent that the scheme remains always stable. At CFL = 1, we observe a damping in the mid-wavenumber range, which depends on the coupled effects of the RK and FD schemes. For higher values of the CFL, the IRS4 operator acts and a double damping peak is visible, which moves towards low wavenumbers as CFL increases. Damping vanishes at smallest scales ($k\Delta x \approx \pi$), which highlights the need for additional high-wavenumber dissipation. Fig. 2(b) shows the amplification factors with artificial dissipation. Since it is added to the spatial operator, its effect is coupled with the temporal scheme, which leads to the non-monotonic behavior for CFL 1 and 2. For high values of CFL, the contractive character of the IRS4 operator dramatically reduces the dissipation, which could also have been inferred from Fig. 1. As a consequence, for CFL $\gtrapprox$ 10, almost no dissipation is applied near the grid cut-off ($k\Delta x \approx \pi$), so that grid-to-grid oscillations can remain undamped and pollute the solution or become unstable. In Fig. 2(c), the selective filtering is applied with a coefficient $\chi = 256/315$, so that the amount of damping is similar to that of AD without IRS. As expected, the spectral characteristics are a combination of the base scheme and the filter response. In particular, the damping at $k\Delta x \approx \pi$ remains the same independently of the CFL value. The fact that the stabilization is independent of the base scheme gives the greater robustness of RK4-IRS4 implementation, notably for high values of CFL, since the filter will continue to dissipate the modes not resolved by the grid. That is why, in the following, the results are obtained with the base scheme supplemented by the selective filtering.

Since the IRS operator essentially introduces a dispersive error, it is also interesting to look at the relative phase error $\phi + \sigma k\Delta x$ in Fig. 3. Since the dissipation term is nondispersive, this quantity is due uniquely to the centered difference operator (4). The striking point in Fig. 3(a) is that IRS4 damages the phase in proportion to the CFL rise. Such a representation would suggest that dispersion errors are unacceptable for CFL greater than 5. However, the analysis would be only valid for a regular grid with constant Δx. In practice, grid points are clustered near wall boundaries, and high values of the CFL (5 or greater) are located at these particular points due to the small Δx. From another point of view, we can also look at the spectral properties relative to a fixed time step Δt, which is done in Fig. 3(b) and (c) for the amplification factor and the phase respectively by multiplying the abscissae by the CFL number σ. For the advection equation, $\omega = k\,a$, and $\sigma\,k\Delta x = \omega\Delta t$. In this representation, it is clear that the base scheme spectral properties are preserved in proportion to the CFL number up to $\omega\Delta t = \pi/2$, i.e. if the time signal is discretized by four or more time steps.

4. Boundary conditions and multi-domain interface treatment

The preceding analysis is valid for an infinite computational domain or a domain with periodic conditions. The modification of the spatial operator close to boundaries will affect both stability and numerical

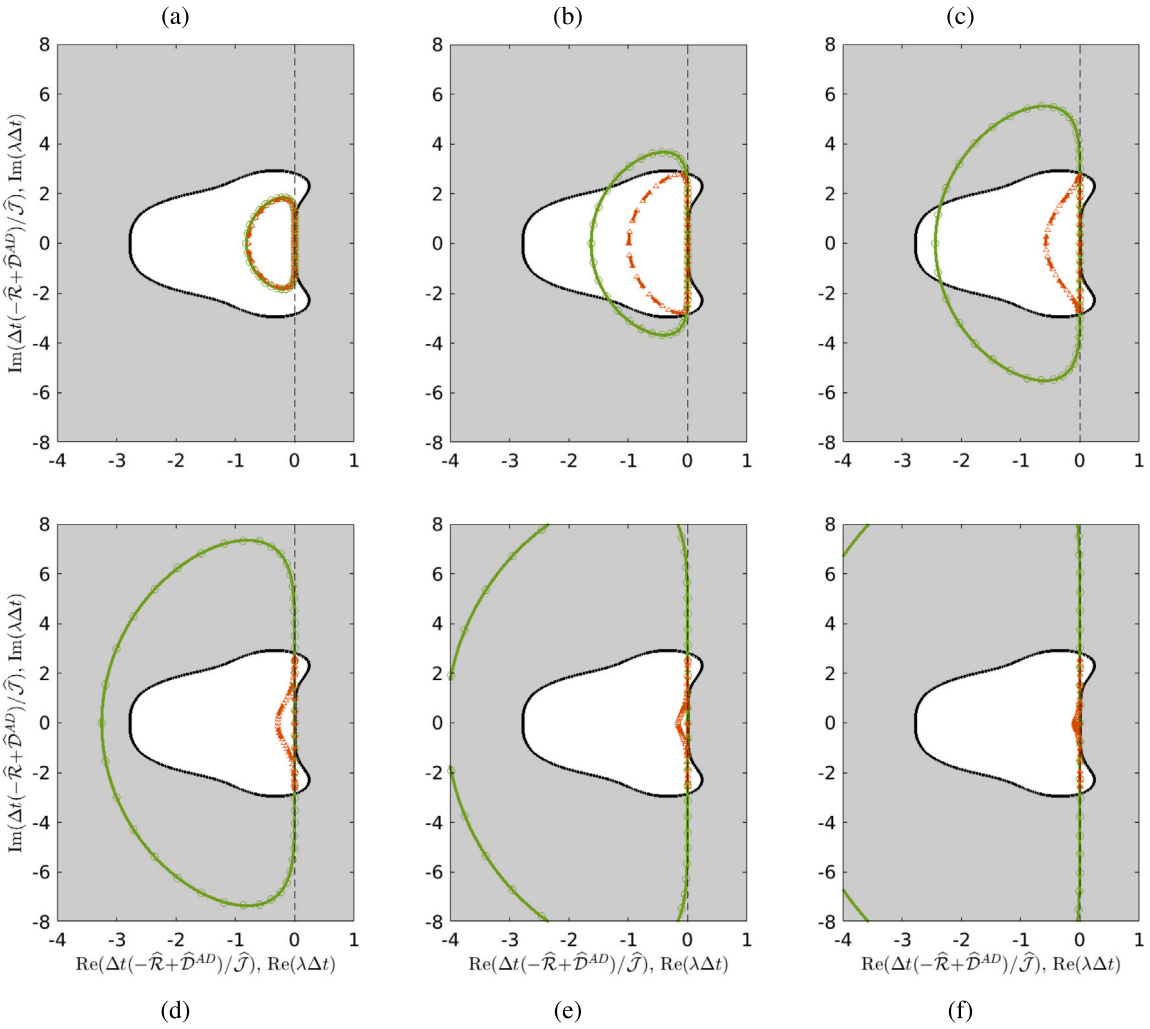

Fig. 1. Stability region of the RK4 (white) and locus of the spatial operator with IRS4 smoothing (red) and without (explicit, green), obtained from the Fourier symbols (lines) and the operator's eigenvalues $\lambda\Delta t$ (symbols). From left to right and top to bottom, CFL = 1, 2, 3, 4, 5 and 6.

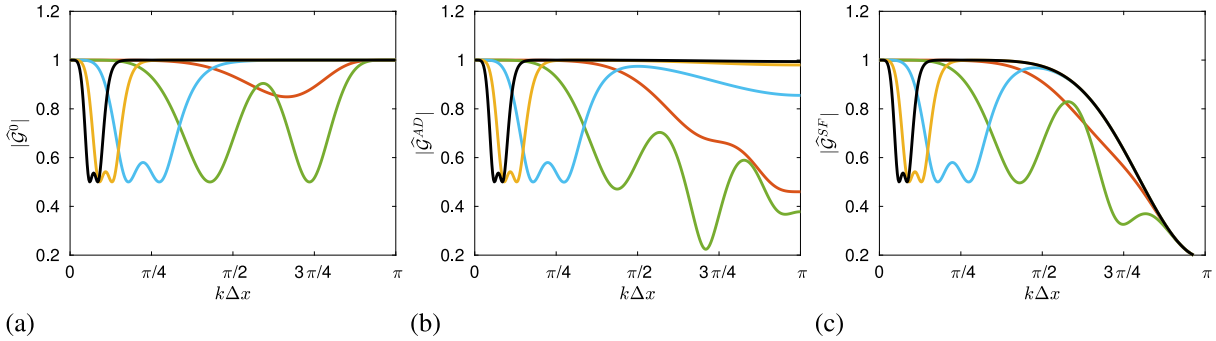

Fig. 2. Amplification factors for the centered spatial operator (a), supplemented by artificial dissipation (b) or by selective filtering (c) for increasing CFL numbers, CFL = 1 (——), 2 (——), 5 (——), 10 (——), 15 (——).

errors. For this reason, the stability analysis in the following will be carried out with the method of lines [38]. For the linear scalar wave problem (14), spatial discretization on a grid with m points yields

$$\frac{\partial \mathbf{w}_m}{\partial t} = -\mathbf{R}_{m,m}\mathbf{w}_m$$

where $\mathbf{w}_m$ is the numerical solution vector, of size m and $\mathbf{R}_{m,m}$ is the matrix associated to the spatial operator $\mathcal{R}$. By taking the Fourier transform of this expression, with $\mathbf{w}_m = \hat{\mathbf{w}}_m e^{\lambda t}$, we obtain the following eigenvalue problem :

$$(a\mathbf{R}_{m,m})\hat{\mathbf{w}}_m = -\lambda\hat{\mathbf{w}}_m \tag{23}$$

4.1. Periodic boundary condition

Writing the IRS scheme at the kth RK stage in matrix–vector form

$$\mathbf{J}_{m,m}\Delta\mathbf{w}_m^{(k)} = -\alpha_k\Delta t\,\mathbf{R}_{m,m}\mathbf{w}_m^{(k-1)}$$

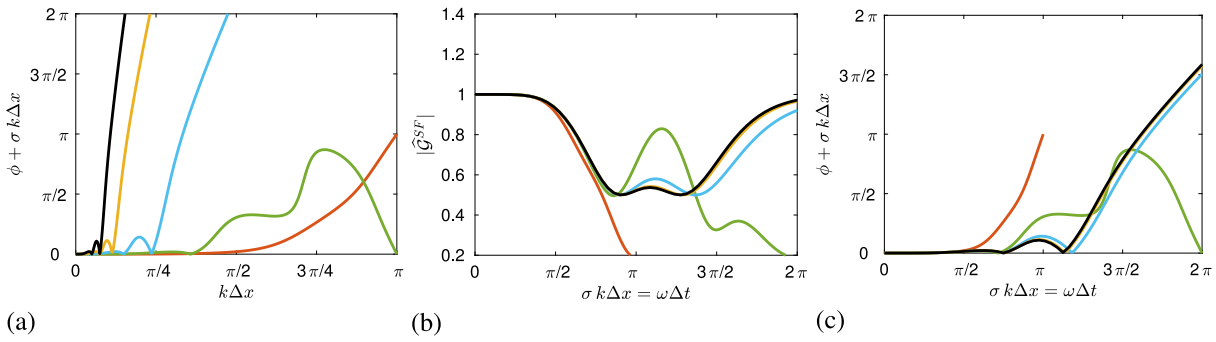

Fig. 3. Spectral properties of IRS4 operator: relative phase error (a), damping factor versus $\omega\Delta t$ (b), and phase error versus $\omega\Delta t$ (c) for increasing CFL numbers, CFL = 1 (——), 2 (——), 5 (——), 10 (——), 15 (——).

the IRS4 operator leads to the inversion of a pentadiagonal matrix $\mathbf{J}_{m,m}$ per direction at each Runge–Kutta stage. For periodic boundary conditions, the periodic matrix $\mathbf{J}_{\mathbf{p}_{m,m}}$ reads:

$$\mathbf{J}_{\mathbf{p}_{m,m}} = \begin{pmatrix} \gamma & \alpha & \beta & 0 & \cdots & \cdots & \cdots & 0 & \beta & \alpha \\ \alpha & \gamma & \alpha & \beta & 0 & \cdots & \cdots & \cdots & 0 & \beta \\ \beta & \alpha & \gamma & \alpha & \beta & 0 & \cdots & \cdots & \vdots & 0 \\ 0 & \beta & \alpha & \gamma & \alpha & \beta & 0 & \cdots & \vdots & \vdots \\ \vdots & \ddots & \ddots & \ddots & \ddots & \ddots & \ddots & \ddots & \ddots & \vdots \\ 0 & \cdots & 0 & \beta & \alpha & \gamma & \alpha & \beta & \cdots & \vdots \\ \vdots & \ddots & \ddots & \ddots & \ddots & \ddots & \ddots & \ddots & \ddots & \vdots \\ 0 & \cdots & \cdots & \cdots & 0 & \beta & \alpha & \gamma & \alpha & \beta \\ \beta & 0 & \cdots & \cdots & \cdots & 0 & \beta & \alpha & \gamma & \alpha \\ \alpha & \beta & 0 & \cdots & \cdots & \cdots & 0 & \beta & \alpha & \gamma \end{pmatrix} \tag{24}$$

with $\beta = \theta_4 \mathrm{CFL}^4$, $\alpha = -4\beta$ and $\gamma = 1 + 6\beta$. The eigenvalue problem (23) then becomes:

$$(\mathbf{J}_{m,m}^{-1}\mathbf{R}_{m,m})\hat{\mathbf{w}}_m = -\lambda\hat{\mathbf{w}}_m \tag{25}$$

For periodic boundary conditions, as expected, the solutions from the eigenvalue problem (25) with IRS4 matrix $\mathbf{J}_{\mathbf{p}_{m,m}}$ perfectly match the locus of the Fourier symbol $\widehat{\mathcal{R}}/\widehat{\mathcal{J}}$, as seen in Fig. 1 for CFL 1 to 6.

4.2. Physical boundary conditions

Near boundaries of the computational domain it is necessary to modify the IRS4 matrix. In Ref. [4], the pentadiagonal matrix is simply truncated, which gives matrix $\mathbf{J}_{\mathbf{1}_{m,m}}$:

$$\mathbf{J}_{\mathbf{1}_{m,m}} = \begin{pmatrix} \gamma & \alpha & \beta & 0 & \cdots & \cdots & \cdots & 0 \\ \alpha & \gamma & \alpha & \beta & \ddots & \cdots & \cdots & 0 \\ \beta & \alpha & \gamma & \alpha & \beta & \ddots & \cdots & 0 \\ 0 & \beta & \alpha & \gamma & \alpha & \beta & \ddots & \vdots \\ \vdots & \ddots & \ddots & \ddots & \ddots & \ddots & \ddots & 0 \\ 0 & \cdots & \ddots & \beta & \alpha & \gamma & \alpha & \beta \\ 0 & \cdots & \cdots & \ddots & \beta & \alpha & \gamma & \alpha \\ 0 & \cdots & \cdots & \cdots & 0 & \beta & \alpha & \gamma \end{pmatrix}, \tag{26}$$

To gain some robustness in the FD implementation, we have chosen to reduce IRS order near boundaries. The second to last row of nodes is smoothed with IRS2 operator of Eq. (9) and the one-sided IRS1 operator [15] is used at the boundary points, yielding matrix $\mathbf{J}_{\mathbf{2}_{m,m}}$:

$$\mathbf{J}_{\mathbf{2}_{m,m}} = \begin{pmatrix} \gamma_1 & \alpha_1 & 0 & \cdots & \cdots & \cdots & \cdots & 0 \\ \alpha_2 & \gamma_2 & \alpha_2 & 0 & \cdots & \cdots & \cdots & 0 \\ \beta & \alpha & \gamma & \alpha & \beta & 0 & \cdots & 0 \\ 0 & \beta & \alpha & \gamma & \alpha & \beta & \ddots & \vdots \\ \vdots & \ddots & \ddots & \ddots & \ddots & \ddots & \ddots & 0 \\ 0 & \cdots & 0 & \beta & \alpha & \gamma & \alpha & \beta \\ 0 & \cdots & \cdots & \cdots & 0 & \alpha_2 & \gamma_2 & \alpha_2 \\ 0 & \cdots & \cdots & \cdots & \cdots & 0 & \alpha_1 & \gamma_1 \end{pmatrix} \tag{27}$$

with coefficients $\alpha_2 = -\theta_2 \mathrm{CFL}^2$ and $\gamma_2 = 1 - 2\alpha_2$ for IRS2, and $\alpha_1 = \pm\theta_1 \mathrm{CFL}$, $\gamma_1 = 1 - \alpha_1$ for IRS1 operator, which is defined as:

$$\begin{cases} \mathcal{J}_{IRS1^+} = 1 - \theta_1 \dfrac{\Delta t}{\Delta x} \lambda^e \delta^+ & \text{for a left boundary} \\ \mathcal{J}_{IRS1^-} = 1 + \theta_1 \dfrac{\Delta t}{\Delta x} \lambda^e \delta^- & \text{for a right boundary} \end{cases} \tag{28}$$

with δ^+, δ^- the upward and backward difference operator respectively. The Fourier symbol of IRS1 and IRS2 are given by:

$$\begin{cases} \widehat{\mathcal{J}}_{IRS1^+} = 1 + 2\,\theta_1 \mathrm{CFL}\left[\sin^2\left(\dfrac{k\Delta x}{2}\right) - i\cos\left(\dfrac{k\Delta x}{2}\right)\sin\left(\dfrac{k\Delta x}{2}\right)\right] \\ \widehat{\mathcal{J}}_{IRS2} = 1 + 4\,\theta_2 \mathrm{CFL}^2 \sin^2\left(\dfrac{k\Delta x}{2}\right) \end{cases} \tag{29}$$

To determine the coefficients θ ensuring the unconditional stability of the different IRS operators, a numerical search is performed for the 1D scalar problem. The results are plotted in Fig. 4. For IRS1, we set the value $\theta_1 = 0.42$. A theoretical value for IRS2 of 1/16 was obtained analytically in [37,39]. In the following, we use the value $\theta_2 = 0.04$, for which the numerical stability is ensured. For IRS4, the distribution of θ_4 as function of CFL follows the same trend as IRS2 with a peak around CFL = 2, where the contractive effect of IRS operator is not yet large. We set the value $\theta_4 = 0.0025$ in the applications.

For a Dirichlet boundary condition, the method of lines is applied with the matrix $\mathbf{J}_{\mathbf{2}_{m,m}}$ and centered schemes with reduced-stencil schemes near boundaries in the spatial operator matrix. The solution increments are imposed at the left boundary so that the corresponding first row and first column are suppressed in the matrices [40]. A simple extrapolation is used at the right boundary. The eigenvalues for m = 200, plotted in Fig. 5 for CFL 2, 5 and 10, show that the locii are significantly modified compared to the old treatment using the truncated matrix $\mathbf{J}_{\mathbf{1}_{m,m}}$. In particular, for the highest CFL value, the use of a reduced stencil IRS operator appears more dissipative, whereas the close-up view in the inset of Fig. 5(right) indicates that some eigenvalues can excite weak instabilities with the truncated version. However, using IRS2 and IRS1 coefficients on the borders, all the eigenvalues have a negative real part so that the linear problem has non growing solutions.

4.3. Interface treatment in multi-domain calculations

4.3.1. The different strategies of parallelization for the linear system resolution

The parallel implementation of IRS is crucial for the efficiency of the method. As we have seen, IRS4 leads to the inversion of a pentadiagonal matrix per mesh direction at each Runge–Kutta step. As the number of linear systems to solve is proportional to the number of implicited directions and to the number of points in that direction, the computational cost can be important. Efficient algorithms, such as Thomas' algorithm or cyclic reduction, exist to solve small-banded matrices on

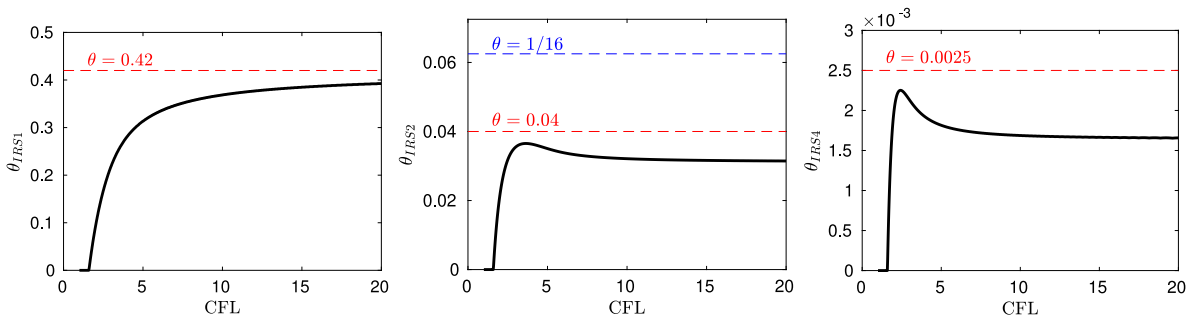

Fig. 4. Numerical determination of smoothing parameter θ ensuring unconditional stability for the 1D advection problem: IRS1 (left), IRS2 (center) and IRS4 (right).

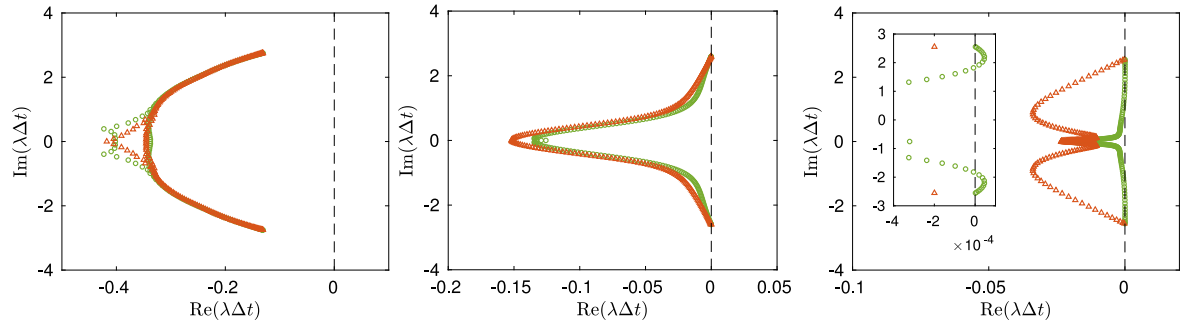

Fig. 5. Eigenvalue spectrum with the method of lines for Dirichlet boundary condition using IRS matrix $\mathbf{J}_{2_{m,n}}$ (△) and $\mathbf{J}_{\mathbf{1}_{m,n}}$ (○): CFL = 2 (left), CFL = 5 (center) and CFL = 10 (right).

scalar computers. They are based on a first forward sweep, during which new coefficients are computed, and then a backward substitution to compute the solution. Unfortunately, such algorithms are hard to parallelize efficiently, even if a large body of literature has tackled this problem, mostly for tridiagonal systems. Strategies based on the redistribution of data between processors [41] or Thomas-pipelined algorithms [42] are better suited for distributed memory architectures, but they lack efficiency due to a large number de communications for the former, and to idle time for the second. Some methods are based on the divide-and-conquer algorithm, where successive transformations are used to divide the original problem over the computing cores. The tridiagonal and banded-matrix solvers available in the ScaLapack library [43] propose an MPI implementation. We have tested the banded-matrix routines of ScaLapack to solve the pentadiagonal systems but the overhead is prohibitive, amounting to approximately 220% with respect to the explicit solver . More complex algorithms, such as Spike [44], have been proposed to reduce the cost. Even if the scalability has been improved, notably for large band matrices on distributed memory or with GPU processors, the cost remains high for pentadiagonal systems. We have also tested the recent PaScal_tdma library [45], which proposes an optimized parallel cyclic reduction method for tridiagonal matrices. The overhead is more reasonable (approximately 30% when few processors per implicit directions are used), but its does not scale well to large number of processors (the overhead increases up to 150% when using about 30 processors per direction); furthermore, the library is not applicable to pentadiagonal matrices. Last but not least, even if each block is individually structured, complex multiblock grids can lead to globally unstructured topologies (see for instance test cases 5.7 to 5.10). In that case, the definition of global linear systems distributed across all blocks is not possible.

Note that the aim here is to relax CFL constrains in compressible DNS and LES, but anyway the maximum allowable time step will be limited by the need of resolving the smallest time scales in the simulation. As shown in Section 5.4, values of CFL of 5 to 10 can then be used for compressible DNS without affecting or reducing the physical time accuracy. Such values are much smaller than those used in steady state simulations ($O(100)$ or more). It is then of the utmost importance that the matrix inversion associated with the implicit treatment is as cheap as possible. For that reason, in the following we extend IRS to parallel and multiblock configurations by solving approximate systems on each subdomains and by truncating the global system to generate local independent linear systems for each processors. Some studies discuss the multi-domain extension for IRS implicitation but are generally restricted to steady problems. Borel and Roux [46] used a Schwarz iterative method for overlapping domain decomposition. They studied the influence of the thickness of the overlap and found an optimal efficiency for an overlapping of $L_0 = 2\text{CFL} + 1$ cells. Lerat and Wu [47] proposed a time-lagging interface condition, where the interface values are fixed at the previous time step. They showed how to obtain a stable and conservative condition. Wu and Zou [48] further analyzed this interface treatment and found an optimal overlap $L_0 = \text{CFL}$ for steady problems. They extended the time-lagging method to unsteady problem by using an overlapping $L_0 = 2\text{CFL} + 1$ points. In Ref. [5], a strategy based on the use of an overlap between blocks was studied by defining halos of ghost points, which is a popular strategy to implement compact FD schemes [49]. It was shown that adding ghost points at the interfaces can limit the error generated by the truncation. This strategy is pursued in the present study.

4.3.2. *The ghost-point strategy*

Layers of ghost cells are used to make mesh blocks independent and reduce the required number of parallel communications. They are filled using the solution increments computed in the neighboring subdomain at the previous RK stage, as schematized in Fig. 6.

In Refs. [4,5], the IRS operator is simply set equal to the identity for the last two rows, which means that the two outside ghost cells are advanced explicitly in time, while the right-hand sides are communicated from the neighboring block. In the present implementation, the coefficients for the two first/last rows in IRS matrix are those of IRS1 and IRS2 operators. For an interior subdomain, the IRS4 matrix is thus $J_{2m+\text{ngh},m+\text{ngh}}$ as defined in Eq. (27) where m is replaced by $m+\text{ngh}$, ngh being the number of ghost cells. Note that the eleven-point stencil base

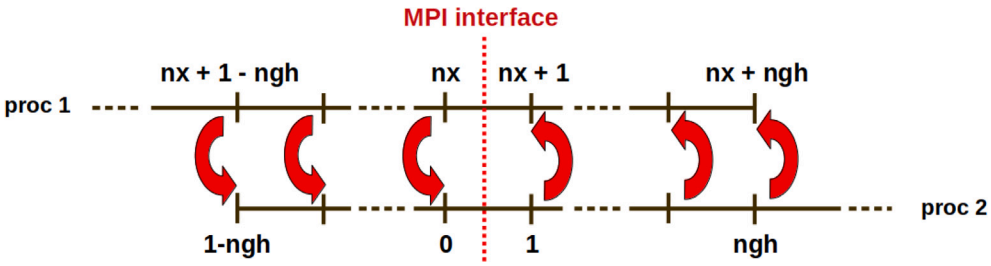

Fig. 6. Schematic of the ghost-point strategy adopted for the parallel implementation of IRS.

schemes already necessitates five rows of ghost points in each direction, so that we use at least ngh = 5. This results in the inversion of a $(m+\text{ngh})\times(m+\text{ngh})$ pentadiagonal matrix per direction on each mesh block, which introduces an overhead. The part due to parallel communications is rather small, and a good parallel scalability is observed for blocks of approximately 50^3 points. The strategy may however suffer from a lack of robustness when using high values of CFL numbers (greater than about 10). To illustrate this point, the scalar advection (14) is solved for a domain $0 < x < 1$ discretized by 600 points. A 1D Gaussian hump, defined as $w(x,0) = \exp(-500(x-0.5)^2)$, is initially located at the middle of the domain and advected periodically to its starting position 10 times at CFL = 5. The results are reported in Fig. 7 using two solutions: the true periodic solution, *i.e.* IRS matrix is $\mathbf{J}_{\mathbf{p}_{m,m}}$ of Eq. (24), and the approximate ghost-point solution, *i.e.* IRS matrix $\mathbf{J}_{\mathbf{2}_{m+\text{ngh},m+\text{ngh}}}$ of Eq. (27). The number of grid points has been chosen so that the periodic hump is correctly advected (some oscillations due to dispersion are visible on its left foot). Then ghost points are used at the left and right boundaries, which can represent the connection with other MPI domains or blocks (note that periodicity is treated as communications by MPI library). Using the nominal number of ghost cells, ngh = 5 (first row of Fig. 7), a numerical instability is observed after 10 turnovers and the simulation blows up rapidly. Using an extended number of ghost cells, ngh = 11 (bottom row of Fig. 7), the solution is in perfect agreement with the periodic one. The corresponding eigenspectra are plotted on the right. Two unstable modes are clearly visible for ngh = 5 and almost disappear for ngh = 11 (weak instabilities with a positive imaginary part of the order of 10^{-9} are present). In fact, numerical waves should not travel at a distance (in terms of the number of mesh points) larger than the one determined by the CFL number at each time step.

Additionally, the above-mentioned simplifications can introduce an error in the interface region. Such an error can be reduced by increasing the number of ghost cells from 5 on each side of the domain to a given integer ngh, so that a reasonable tradeoff between cost and accuracy has to be found. Previous analyses by Wu and Zou [48] for a time-lagging interface condition suggest that "since the CFL number is based on the maximum wave speed (eigenvalue), it is natural that a local perturbation (due to time-lagging) of the scheme will travel at a distance, in terms of the number of mesh points, no larger than the CFL number at each time step". An optimal overlapping width of 2CFL + 1 would enable to contain the error in the overlapping region. As a consequence, the overlapping method using ghost points should maintain the order of accuracy of the interior scheme if ngh≈2CFL + 1. This point will be investigated in Section 5.3 for a vortex advection problem. In practice, all following applications are run on parallel computers. The maximum CFL is tested for each interface and the number of ghost points is set to max(5,2CFL + 1). Generally, high CFL region are located near wall boundaries and few interfaces are concerned by the ghost-point extension.

5. Applications to compressible Navier–Stokes equations

5.1. Governing equations

The compressible Navier–Stokes equations are written for a curvilinear domain by using a coordinate transform. The physical space (x, y, z) is mapped into a Cartesian regular computational space (ξ, η, ζ). By denoting $\mathbf{u} = (u, v, w)^T$ the velocity vector, ρ the density, p the pressure and E the total specific energy, the set of equations for the unknown vector $\mathbf{U} = (\rho, \rho u, \rho v, \rho w, \rho E)^T$ is given by:

$$\frac{\partial \mathbf{U}}{\partial t} + \frac{1}{J}\left(\frac{\partial \mathbf{F}_c}{\partial \xi} + \frac{\partial \mathbf{G}_c}{\partial \eta} + \frac{\partial \mathbf{H}_c}{\partial \zeta}\right) = 0 \tag{30}$$

with $J = \partial(x,y,z)/\partial(\xi,\eta,\zeta)$ the Jacobian of the coordinate transformation. The curvilinear fluxes are $\mathbf{F}_c = \mathbf{F}_c^e - \mathbf{F}_c^v$, $\mathbf{G}_c = \mathbf{G}_c^e - \mathbf{G}_c^v$, $\mathbf{H}_c = \mathbf{H}_c^e - \mathbf{H}_c^v$, where the inviscid (superscript e) and visco-thermal fluxes (superscript v) are given by:

$$\begin{aligned}
\mathbf{F}_c^e &= J\begin{pmatrix} \rho\Theta_\xi \\ \rho\mathbf{u}\Theta_\xi + p\nabla\xi \\ (\rho E + p)\Theta_\xi \end{pmatrix}, \quad \mathbf{G}_c^e = J\begin{pmatrix} \rho\Theta_\eta \\ \rho\mathbf{u}\Theta_\eta + p\nabla\eta \\ (\rho E + p)\Theta_\eta \end{pmatrix}, \\
\mathbf{H}_c^e &= J\begin{pmatrix} \rho\Theta_\zeta \\ \rho\mathbf{u}\Theta_\zeta + p\nabla\zeta \\ (\rho E + p)\Theta_\eta \end{pmatrix}, \\
\mathbf{F}_c^v &= \begin{pmatrix} 0 \\ \boldsymbol{\tau}_\xi \\ \mathbf{u}\cdot\boldsymbol{\tau}_\xi - \mathbf{q}\cdot\nabla\xi \end{pmatrix}, \quad \mathbf{G}_c^v = \begin{pmatrix} 0 \\ \boldsymbol{\tau}_\eta \\ \mathbf{u}\cdot\boldsymbol{\tau}_\eta - \mathbf{q}\cdot\nabla\eta \end{pmatrix}, \\
\mathbf{H}_c^v &= \begin{pmatrix} 0 \\ \boldsymbol{\tau}_\zeta \\ \mathbf{u}\cdot\boldsymbol{\tau}_\zeta - \mathbf{q}\cdot\nabla\zeta \end{pmatrix},
\end{aligned} \tag{31}$$

where $\Theta_\xi = \mathbf{u}\cdot\nabla\xi$, $\Theta_\eta = \mathbf{u}\cdot\nabla\eta$, and $\Theta_\zeta = \mathbf{u}\cdot\nabla\zeta$ are the contravariant velocities. We have noted $\boldsymbol{\tau}_\xi = D\cdot\nabla\xi$, $\boldsymbol{\tau}_\eta = D\cdot\nabla\eta$, and $\boldsymbol{\tau}_\zeta = D\cdot\nabla\zeta$, where D is the viscous stress tensor. The specific total energy is $E = p/[(\gamma-1)\rho] + (u^2+v^2+w^2)/2$ for an ideal gas satisfying $p = \rho r T$, where T the temperature, r the gas constant and γ the ratio of specific heats. The tensor tensor D follows the Newtonian fluid constitutive relation. The dynamic viscosity μ is approximated with Sutherland's law and the heat flux components are modeled with Fourier's law, $\mathbf{q} = -\kappa\nabla T$, κ being the thermal conductivity, modeled by a constant Prandtl number (Pr) assumption.

5.2. Implementation in MUSICAA code

All the numerical schemes are implemented within the MUSICAA code (MUltiblock solver IN computational Aerodynamics and Aeroacoustics), developed at DynFluid laboratory, which is a high-fidelity finite-difference solver written in Fortran and parallelized with MPI library. To optimize computational and memory requirements, three sub-solvers are implemented: (i) for Cartesian grids, the Navier–Stokes equations are directly written in conservative form for Cartesian coordinates (x, y, z); (ii) for 2D curvilinear grids, (x, y) is transformed into (ξ, η), and the third direction, which corresponds generally to the spanwise direction z, is left unchanged (see equations in [50]); (iii) for fully 3D curvilinear grids, the system (30) is solved. The metrics for nonuniform grids are computed using the same finite-difference scheme as the one used for the discretization of fluxes. In particular, a great care is taken

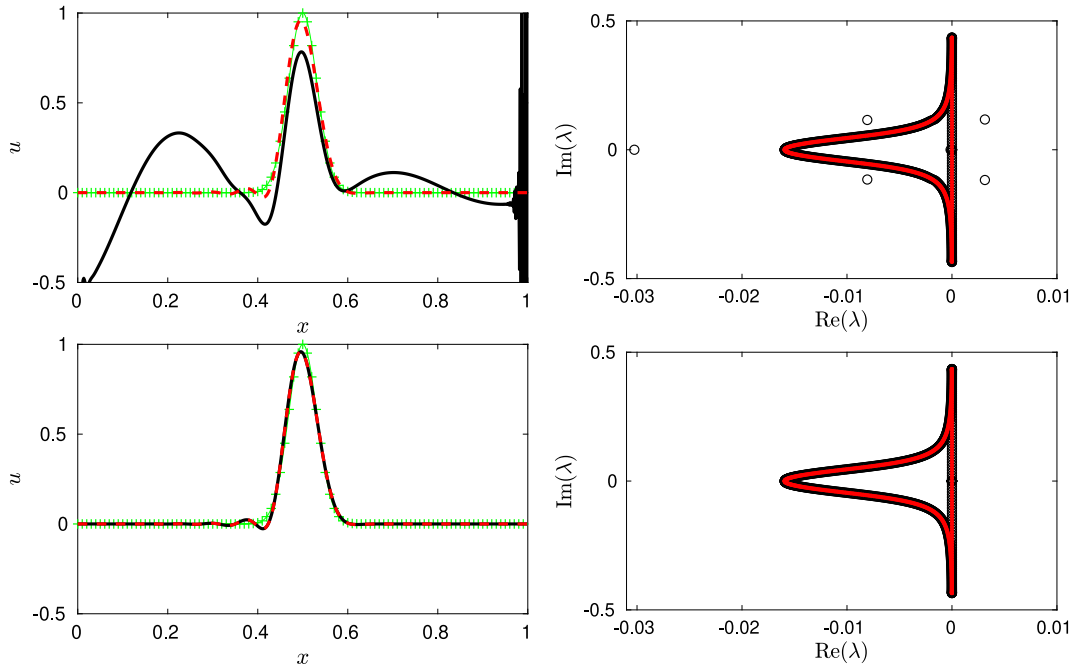

Fig. 7. Scalar advection of a Gaussian hump: On the left, the solutions after 10 turnovers at CFL = 5 using true periodic conditions (– – –) and the approximate conditions with ghost points (———) are compared to the initial (exact) solution (++). The corresponding eigenspectrum is given on the right with red symbols for the periodic problem et black symbols for the ghost-point problem. For top figures, ngh = 5 and for bottom figures, ngh = 11.

to ensure metrics commutation in 2D and metrics conservation in 3D, using the geometric conservation law (GCL) [51,52].

Various spatial and temporal schemes are available in MUSICAA but we restrict the attention for the present applications to the tenth-order FD and four-stage RK scheme, previously presented in Section 2. Fourth-order central differencing is used for viscous fluxes, which are integrated in the last RK substep (this choice is discussed in Section 5.5). For wall boundary conditions, the no-slip condition $u = v = w = 0$ is enforced together with the nullity of the normal pressure gradient. The temperature is also prescribed, either directly for isothermal walls or from the nullity of normal temperature gradient for adiabatic walls, so that all variables are imposed and the increment is zero for IRS matrix at the wall points. The FD scheme is reduced down to second order near walls. In the following test-cases, at free boundaries, non-reflecting Tam and Dong's conditions [53] are applied on the first 5 rows of cells. One-sided 7 point-stencil FD schemes [53] are applied for derivatives normal to borders, and the resulting discretized terms are added to the increments before smoothing.

Except if otherwise specified, the tenth-order filtering is applied after the smoothing with $\chi = 0.2$, as explained in Section 3.3, and the nominal implicit residual smoothing coefficients are $\theta_1 = 0.42$, $\theta_2 = 0.04$ and $\theta_4 = 0.0025$. Using 2D coordinate transform $(\xi, \eta, z) \to (x, y, z)$, the multi-dimensional IRS4 operator is written as:

$$\mathcal{J} = \left(1 + \theta_4 \left(\frac{\Delta t}{\Delta \xi}\right)^4 \delta_\xi (\lambda^e_{\xi\eta}{}^4 \delta^3_\xi)\right)\left(1 + \theta_4 \left(\frac{\Delta t}{\Delta \eta}\right)^4 \delta_\eta (\lambda^e_{\xi\eta}{}^4 \delta^3_\eta)\right) \times \left(1 + \theta_4 \left(\frac{\Delta t}{\Delta z}\right)^4 \delta_z (\lambda^{e4}_z \delta^3_z)\right) \tag{32}$$

noting that the transformed coordinates (ξ, η) correspond to a unitary Cartesian grid ($\Delta\xi = \Delta\eta = 1$). The subscript of the difference operator δ denotes the grid direction in which it is applied. In the z-direction, the directional spectral radius of the inviscid Jacobian matrix is $\lambda^e_z = |w| + c$, c being the local sound speed. Since the transformed directions are coupled, a single spectral radius is used for (ξ, η)-directions (in the spirit of Pulliam [54] for artificial dissipation):

$$\lambda^e_{\xi\eta} = \sqrt{\Theta^2_\xi + \Theta^2_\eta} + c\sqrt{\nabla\xi^2 + \nabla\eta^2}\,, \tag{33}$$

For fully 3D curvilinear grids, the IRS4 operator reads

$$\mathcal{J} = \left(1 + \theta_4 \left(\frac{\Delta t}{\Delta \xi}\right)^4 \delta_\xi (\lambda^e_{\xi\eta\zeta}{}^4 \delta^3_\xi)\right)\left(1 + \theta_4 \left(\frac{\Delta t}{\Delta \eta}\right)^4 \delta_\eta (\lambda^e_{\xi\eta\zeta}{}^4 \delta^3_\eta)\right) \times \left(1 + \theta_4 \left(\frac{\Delta t}{\Delta \zeta}\right)^4 \delta_\zeta (\lambda^e_{\xi\eta\zeta}{}^4 \delta^3_\zeta)\right) \tag{34}$$

with the following spectral radius coupling the three space directions:

$$\lambda^e_{\xi\eta\zeta} = \sqrt{\Theta^2_\xi + \Theta^2_\eta + \Theta^2_\zeta} + c\sqrt{\nabla\xi^2 + \nabla\eta^2 + \nabla\zeta^2} \tag{35}$$

The number of ghost cells ngh required in domain interfaces and the switch (7) for the filtering coefficient are based on the local CFL, defined as

$$\mathrm{CFL}_{\mathrm{local},i} = \Delta t(\Theta_\xi + c\nabla\xi); \quad \mathrm{CFL}_{\mathrm{local},j} = \Delta t(\Theta_\eta + c\nabla\eta);$$
$$\mathrm{CFL}_{\mathrm{local},k} = \Delta t(\Theta_\zeta + c\nabla\zeta)$$

where i, j, k denote the three directions.

5.3. Vortex advection

As noted earlier, the major issue in multi-domain computations is the treatment of interfaces between domains. In the present work, communication between adjacent meshes is conducted through finite-size overlaps. Their effect on solution accuracy and stability is investigated initially for the unsteady inviscid flow generated by a vortex convected by a uniform flow with freestream Mach number $M = U_\infty/c = 0.5$. The initial condition is determined from Taylor's theoretical vortex model:

$$\begin{cases} u = U_\infty + A\dfrac{y}{\Delta y}\exp(\alpha R^2) \\ v = -A\dfrac{x}{\Delta x}\exp(\alpha R^2) \\ p = p_\infty - \rho_\infty \dfrac{A^2}{4\alpha\Delta x\Delta y}\exp(2\alpha R^2) \end{cases} \tag{36}$$

where $R = \sqrt{(x - x_0)^2 + (y - y_0)^2}$ with $(x_0, y_0) = (-30, 0)$ the initial vortex position, using a reference length $L = 1$ m. The vortex strength is $A = 5$ and $\alpha = -\ln 2/b^2$, where the Gaussian half-width is set to $b = 4$. The computational domain $-100 < x < 100$, $-100 < y < 100$ is

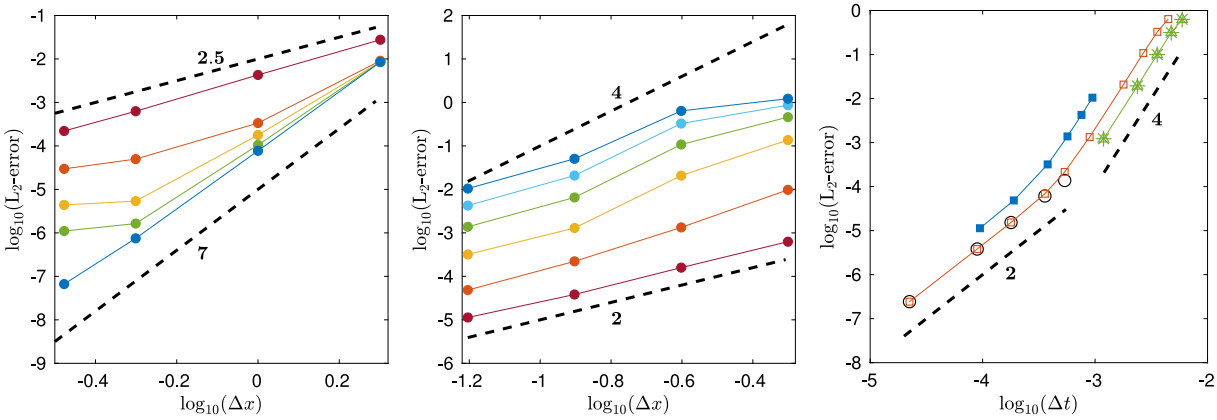

Fig. 8. Vortex advection: L_2-norm of the error with respect to the analytical solution. Left, error of the explicit solver as a function of the mesh size Δx (grids 50 × 50, 100 × 100, 200 × 200, 300 × 300) for small CFL numbers (•, 1; •, 0.5; •, 0.1; •, 0.1; •, 0.02). Middle, error of the IRS4 solver as a function of the mesh size Δx (grids 200 × 200, 400 × 400, 800 × 800, 1600 × 1600) for large CFL numbers (•, 1; •, 2; •, 4; •, 6; •, 8; •, 10). Right, error as a function of the time step Δt: explicit solver (○) and IRS4 solver (□) for the grid 400 × 400 on 4 blocks at $M = 0.5$; IRS4 solver on grid 400 × 400 at $M = 0.1$ on 4 blocks (△) and 1 block (∗); IRS4 solver on grid 1600 × 1600 at $M = 0.5$ (■).

discretized by $N \times N$ uniformly spaced points, and periodic conditions are enforced in both directions. The grid is subdivided into four equally sized subdomains. The vortex, initially located on the interface $y = 0$, is advected from left to right during 100 time units L/U_∞, crossing the interface located at $x = 0$. The L_2-norm of the error with respect to the analytical solution is first used to assess the solver accuracy. The first series of runs, reported on the left of Fig. 8, uses low CFL values between 0.02 and 1 with explicit time marching and deliberately coarse grids ranging between $N = 50$ to 300 to distinguish the accuracy of the spatial scheme. A slope of 2.5 in the log–log plot is obtained at CFL = 1 and a very small time step has to be used to approach the spatial scheme accuracy. A slope of 7 is obtained for CFL = 0.02. This first series shows that the temporal error rapidly dominates for this advection case.

In the second series of runs (middle plot of Fig. 8), the IRS4 solver is used for large CFL numbers between 1 and 10 on fine grids ($N = 200$ to 1600) to highlight temporal integration errors. At CFL = 1, the second-order accuracy of RK4 for nonlinear problems is recovered, and the slope slightly increases for higher CFL. The error saturates for the coarsest grids and CFL 8 to 10, since the error level is very high and the vortex is severely damaged during its advection.

Finally in the right subfigure of Fig. 8, error logarithm is plotted as function of logarithm of Δt for the grid 400 × 400 and CFL ranging from 0.1 to 10 with IRS4 smoothing. Up to CFL 1.2 the error is the same as the one obtained with the explicit solver (black circles) and the solution is second-order accurate. For higher values, a steeper slope of 4 is observed since the advection error rapidly rises when coarsening the mesh. By reproducing the same numerical experiment with a very fine grid ($N = 1600$) for CFL 1, 2, 4, 6, 8, 10 (filled squares), it is clear that the change of slope is due to the difficulty to advect information with large time steps. A last test for the large CFL values is realized with $N = 400$ for a lower Mach number, $M = 0.1$. The error levels are the same as the ones obtained for $M = 0.5$. For these runs, a single domain was also used, which does not change the measured error, meaning that the errors are not related to the interface treatment.

In the preceding tests, the number of ghost cells for the MPI domain overlaps has been set to 2CFL + 1. The influence of the number of ghost cells is illustrated in Fig. 9 for $N = 1600$ and CFL = 10. We report the iso-contours of the fluctuating pressure field, obtained by varying the number of ghost cells from 6 to 18. Intense spurious noise is generated when 6 ghost cells are used (note that the simulation blows up for 5 ghost cells). The spurious acoustic pulse and the vertical and horizontal oscillations developing at the interfaces are reduced for 9 ghost cells and are almost absent when 18 ghost cells are used (the theoretical value is 2CFL + 1 = 21).

Table 1
Numerical parameters and computational performance of turbulent channel flow simulations with and without IRS4.

Case	Δt^+	Nb iterations	$\frac{t_{\text{cpu,expl}}}{t_{\text{cpu}}}$	Time/it	Legend
EXPL CFL = 1	1.05×10^{-2}	750 000	1.0	1.0	
IRS4 CFL = 4	4.21×10^{-2}	187 000	3.30	1.18	
IRS4 CFL = 5	5.26×10^{-2}	150 000	4.06	1.18	
IRS4 CFL = 6	6.31×10^{-2}	125 000	5.08	1.18	▽
IRS4 CFL = 7	7.36×10^{-2}	110 000	5.93	1.18	○

5.4. DNS of turbulent channel flow

The increased stability achieved through IRS4 smoothing is particularly beneficial for the simulation of wall-bounded turbulent flows, where very small mesh sizes are required near the wall to capture the stiff velocity gradient and predict the wall friction accurately. The first case investigated is the turbulent channel flow at Reynolds number $Re_\tau = (\rho_w u_\tau H)/\mu_w = 180$, based on the friction velocity u_τ, the channel half-height H and the wall density and viscosity ρ_w and μ_w, respectively. The computational domain of $4\pi H \times 2H \times 2\pi H$ is discretized with a grid 192 × 180 × 160, uniformly spaced in the homogeneous directions x and z and clustered at the wall in the wall-normal direction y. This leads to a DNS resolution of $\Delta x^+ = 11.9$, $\Delta z^+ = 7.1$, $\Delta y_w^+ = 0.8$ and $\Delta y_c^+ = 4$, where the subscripts w and c are used to denote the wall and centerline resolutions, respectively. Isothermal no-slip conditions are applied at the walls and periodicity conditions along the streamwise and spanwise directions. The Mach number is set to $M = 0.3$ and the simulations are parallelized on 80 cores. For the implicit cases, IRS4 is applied in the wall-normal direction only, and the number of ghost points used for the IRS4 at the MPI interfaces is set to 5, i.e. the minimum required by the scheme stencil. Results using an explicit time integration with a global time step Δt_{expl} are compared with IRS4-accelerated simulations using time steps ranging from $4\Delta t_{expl}$ to $7\Delta t_{expl}$ (see Table 1).

In the explicit case, the maximum CFL number is chosen equal to 1 to ensure stability throughout the simulation. Choi & Moin [55] studied the effects of the computational time step on the numerical solutions for an incompressible turbulent channel flow at $Re_\tau = 180$ using a fully implicit method. Up to $\Delta t^+ = 0.4$, no significant deterioration of turbulence statistics was observed. For the case IRS4 CFL = 7, which corresponds to the highest CFL used here, the time step is equal to 0.0736, well below the limit found in [55], so we expect the physical time step to have little impact on the accuracy of the solution. This allows to observe the influence of additional numerical errors introduced by the IRS4 on the solution quality. For all implicit cases, the total

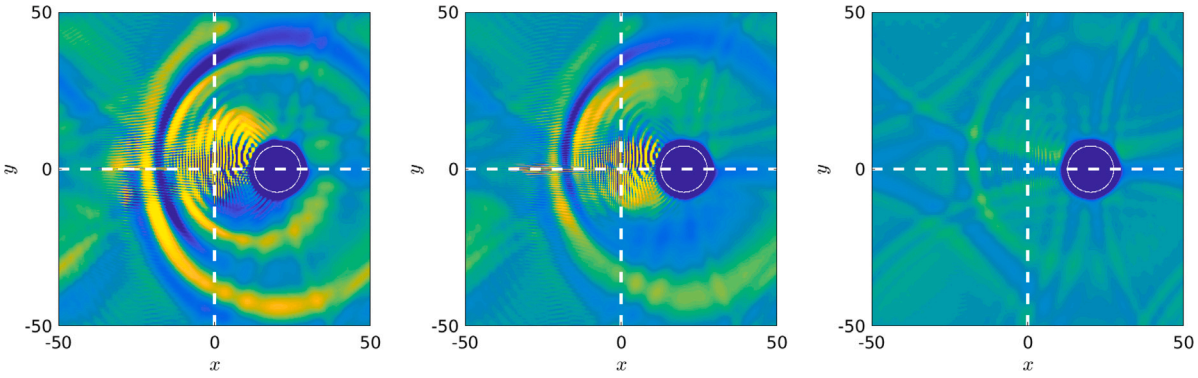

Fig. 9. Vortex advection: maps of fluctuating pressure (between ±5 Pa, and 1 white contour for −100 Pa identifying the vortex core) on the grid 1600 × 1600 and CFL = 10 using 6 (left), 9 (center) and 18 (right) ghost points. The white dashed lines mark the domain interfaces.

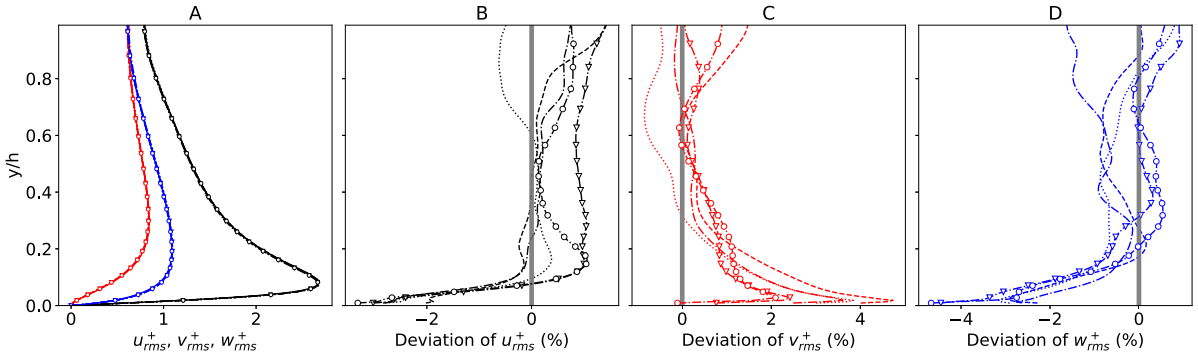

Fig. 10. Turbulent channel flow: comparison of the rms velocities profiles (u^+_{rms}, v^+_{rms} and w^+_{rms}) with the Vreman & Kuerten (——) Ref. [56] for the explicit and IRS4 time integration cases. Line legends in Table 1.

number of iterations used to reach a statistically converged solution corresponds to the total number of iterations of case EXPL divided by CFL, so that the statistics are collected over the same physical time interval for all cases. Comparisons of the computational cost for the explicit and implicit cases show that applying IRS4 in the wall-normal direction represents an overhead of 18% per iteration. However, the total number of iterations being reduced proportionally to the CFL in use, the total computation time is reduced. For instance a reduction by a factor 4.06 is obtained for CFL = 5, and a factor 5.93 is found for CFL = 7.

Fig. 10 shows numerical solution for the various cases at stake. These are compared to the reference solution of Vreman & Kuerten [56], obtained with an incompressible solver based on spectral method and a very fine grid. The root-mean-square (rms) velocities profiles are plotted in Fig. 10(A) along with the reference solution and we observe a very good agreement for all cases. To highlight differences, the relative deviations from the reference are plotted Fig. 10(B, C and D). These are defined as $\mathrm{dev}(u^+_{i,rms}) = (u^+_{i,rms,\mathrm{VK}} - u^+_{i,rms})/u^+_{i,rms,\mathrm{VK}}$ with $u^+_{i,rms,\mathrm{VK}}$ the solution of Vreman & Kuerten for the ith velocity component. Except for points close to the wall, deviations are below 1% for all cases. Moreover, the application of the IRS4 does not lead to any noticeable increase of the relative deviation. For an accumulation of statistics on an equivalent duration, we observe a good convergence of second-order statistics with a reduced computational cost when applying IRS4. For simulations that require a longer time to converge statistics or to obtain higher-order statistics, introducing IRS4 acceleration is therefore particularly beneficial.

5.5. LES of real-gas turbulent boundary layers

As a second application, we consider boundary-layer transition of a real gas at high-subsonic condition (Mach 0.9). For this spatially evolving configuration, timestep constraints for DNS resolution of the wall-bounded turbulence are similar to those encountered in the channel flow case. In the laminar and transitional regimes, growing instability waves are particularly sensitive to dispersion errors, whereas numerical resolution of the turbulent region strongly depends on numerical dissipation. A modal transition is performed by injecting at the flow inlet plane a pair of oblique modes skewed by 30° with respect to the streamwise direction and with a nondimensional angular frequency $\omega_0 L^*/U_\infty = 0.02$. The inlet Reynolds number Re_{L^*} based on Blasius length $L^* = x/\sqrt{Re_x}$ is equal to 1000. The spanwise extent is taken equal to one spanwise wavelength of the input modes, $\lambda_z = 2\pi/\beta_0$, with the spanwise wavenumber $\beta_0 = 0.04L^*$. Adiabatic no-slip conditions are applied at the wall, and non-reflecting Tam & Dong's conditions are imposed at the inlet, top and outflow boundaries. The working fluid is perfluorinated ketone Novec649, a dense gas used in energy conversion systems, and specifically Organic Rankine Cycles (ORC). The thermodynamic flow conditions correspond to a freestream temperature of 100 °C and a pressure of 4 bars. At such conditions, the fluid deviates from ideal gas behavior. Real-gas effects are modeled with the Peng–Robinson–Stryjek–Vera equation of state [57] and the Chung-Lee-Starling model [58] for the transport properties.

First, a DNS with the explicit time integration is realized over a computational grid of 9000 × 400 × 1000 points, achieving a total of 3.6 billions points parallelized on 16 384 processors. The resolution in wall units corresponds to $\Delta x^+ = 14$ in the streamwise direction, $\Delta z^+ = 7$ in the spanwise direction, and $\Delta y^+_w = 0.7$ and $\Delta y^+_e = 11$ at the wall and at the boundary-layer edge, respectively. The grid is uniform in the streamwise direction and the spanwise direction, and streched in the direction normal to the wall by a factor of 1.015 up to the 190th point. The streamwise domain extends up to a momentum-thickness Reynolds number $Re_{\theta,end} \sim 5000$, allowing the observation of high Reynolds-number effects. Despite the high subsonic Mach number, we found that the mean and fluctuating turbulent profiles are very close to

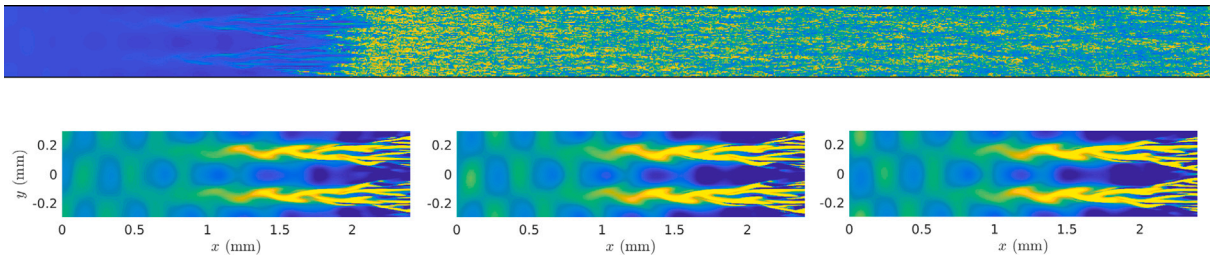

Fig. 11. Instanteaneous view of the streamwise velocity at $y^+ \approx 15$ for the DNS of real-gas boundary-layer flow over the full domain (top). Close-up view of the fluctuating streamwise velocity in the transition region for DNS (left), LES-expl (middle) and LES-IRS4 (right).

Table 2
Characteristics of the different cases for the real-gas turbulent boundary layers.

Case	CFL	$\Delta t/\Delta t_{\text{DNS}}$	Filter/IRS	visc.	Δx^+	Δy^+_w	Δy^+_e	Δz^+	$Re_{\theta,end}$	Legend
DNS	1	1.00	Outside	Last	14	∼0.7	∼11	7	∼5000	
LES-expl	1	1.33	Outside	Last	28	∼0.8	∼14	11	∼3300	
LES-IRS4	4	5.33	Outside	Last	28	∼0.8	∼14	11	∼3300	
LES-IRS4-inc	4	5.33	Inside	Last	28	∼0.8	∼14	11	∼3300	
LES-IRS4-visc	4	5.33	Outside	All	28	∼0.8	∼14	11	∼3300	

incompressible DNS databases, essentially due to the high specific heat of Novec649 which significantly reduces friction heating at the wall.

Second, several LES are carried out for the same conditions as the DNS, in order to validate our LES/IRS strategy. The LES computational grid, composed by $9000 \times 400 \times 1000$ points (712 millions), is obtained by reducing the resolution and the streamwise length (see Table 2). We chose a wall-resolved implicit large eddy simulation strategy, whereby the explicit selected filter ensures selective regularization of the sub-filter turbulent scales. This implicit modeling strategy has been shown to be effective [27] and avoids the computational overhead introduced by the explicit subgrid-scale models. The first LES, using explicit time marching at $\text{CFL}_{max} = 1$ is referred to as LES-expl hereafter and is used to validate our wall-resolved LES strategy, in particular the resolution and the implicit subgrid model. For the second LES, called LES-IRS4, the IRS4 smoothing is applied in the wall-normal direction with a CFL_{max} of 4, resulting in CPU time reduction by a factor 3.5 with respect to the explicit case. The number of ghost cells for IRS parallelization is ngh = 5 and the selective filtering operation is applied after the smoothing, as proposed in Section 3.3. A third LES (LES-IRS4-inc) is performed to assess the latter modification. The filtering is applied and added to increments before residual smoothing. This is the case in the previous implementation [4,5]. Finally, as explained in Section 5.2, for all viscous computations, considering the slower evolution time of viscous terms, the latter are integrated in the last substep of RK4. The fourth LES (LES-IRS4-visc) is used to validate this point, by reproducing LES-IRS4 with an integration of viscous terms at all RK substeps. The main characteristics of the different simulations are summarized in Table 2 (for more details, the reader is referred to [59]). A snapshot of the boundary-layer transition is reported in Fig. 11. In the close-up views of the fluctuating velocity near the wall, plotted with the same color levels, we can see that the transition pattern (with streak doublings) is very similar for DNS and LES with or without IRS4.

Since the turbulent boundary layer velocity field exhibits an incompressible-like behavior due to the high specific heat of the real gas, the results are compared with the incompressible DNS of Schlatter and Örlü [60]. Results for the friction coefficient C_f are reported in Fig. 12. The C_f evolution of LES-expl and LES-IRS4 calculations are in very good agreement with the DNS, including the location of the transition. We focus in the following on the turbulent boundary layer at the location $Re_\theta = 3270$. The turbulent intensity profiles are reported in Fig. 12. A good match with the DNS and the incompressible reference is observed, with a slight underestimation of turbulent intensities, due to the LES resolution. The profiles for LES-expl and LES-IRS4 are almost superimposed, demonstrating the accuracy of the implicit time advancement. The results for the two supplementary LES (LES-IRS4-inc and LES-IRS4-visc) are not represented for clarity since they are superimposed on those of LES-IRS4.

To investigate in more detail the differences between the cases, the spanwise and temporal spectra of the streamwise velocity fluctuations are plotted in Fig. 13. As expected, the premultiplied spanwise spectra for LES cases exhibit an earlier cut-off due to coarser spanwise resolution. Interestingly, we observe a better resolution of LES-IRS4 w.r.t LES-expl at the small scales. This is a consequence of the lower numerical dissipation introduced in LES-IRS4, because numerical dissipation is applied less frequently over the integration interval, due to the larger time step. Similar results are obtained for the temporal spectra. This means that the LES cut-off is governed by streamwise resolution and not by time resolution. We can notice a smoother decaying slope for LES-IRS4, most likely due to the dispersion of the IRS4 operator. Finally, the temporal spectra for the two supplementary LES (LES-IRS4-inc and LES-IRS4-visc) are compared with LES-IRS4 in Fig. 13 (right). Symbols have been added but the spectra are almost undistinguishable. This validates two issues: (i) filtering before or after the smoothing operation has no incidence on the results but only on the stability, where filtering after smoothing is preferable to avoid that the contractive effect of IRS suppresses the necessary numerical dissipation; (ii) integrating viscous terms at the last RK step does not change the results (at least for problems not fully dominated by viscous effects) and allows a substantial reduction of computing time.

5.6. Laminar flow past a cylinder

We now investigate the performance of IRS4 on curvilinear grids. The first test problem is the unsteady laminar flow around a 2D circular cylinder at a Mach number $M = 0.3$ and a Reynolds number $Re_D = 1200$, based on cylinder diameter D and freestream velocity U_∞. Even if the flow is expected to become three-dimensional at the selected Reynolds number, this configuration remains a good numerical test case used in the literature to assess the performance of numerical schemes [61,62]. In the aim of observing the influence of time integration errors, a relatively fine grid of 360×300 points is selected. An O-grid is generated with a first mesh size at the wall of $0.0028D$, and free boundary located at a distance of $20D$. Grid points are uniformly distributed in the azimuthal direction. Tam & Dong's non-reflecting conditions are used at the free boundary and an adiabatic no-slip condition is prescribed at the wall. The initial flow is symmetric and the transient phase is run with the explicit solver ($\text{CFL}_{max} = 0.5$, $\Delta t U_\infty / D = 2.76 \times 10^{-4}$) during 600 000 iterations. The recirculation bubble behind

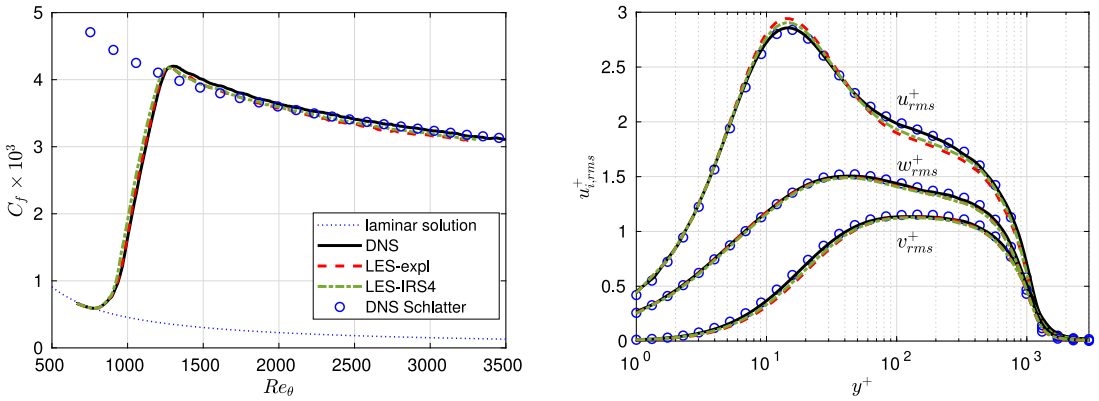

Fig. 12. Skin friction coefficient (left) and rms velocities profiles at Re_θ = 3270 (right) for the different cases and the DNS of Schlatter and Örlü [60].

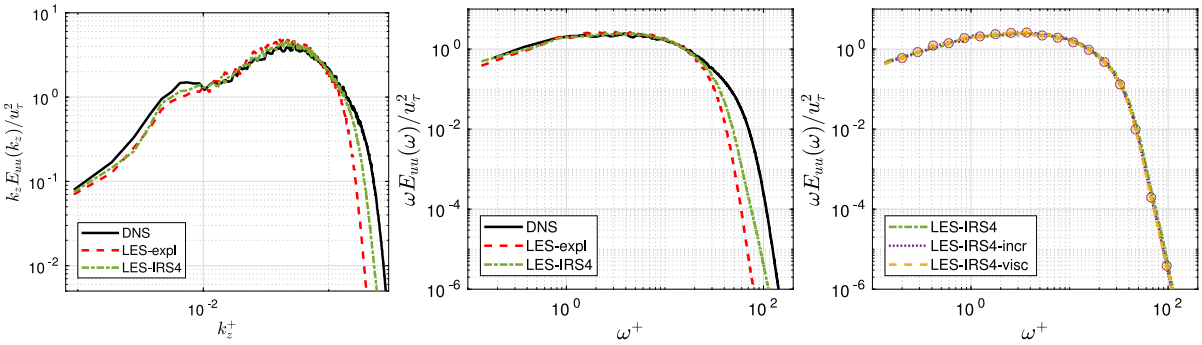

Fig. 13. Premultiplied spanwise (left) and temporal (middle,right) spectra of the streamwise velocity fluctuations for the turbulent boundary layer at Re_θ = 3270.

Table 3
Laminar flow past a cylinder: Simulation and flow parameters (percentage errors in parentheses with respect to expl CFL = 0.5).

Case	Iterations	ngh	Time/it	$t_{\text{cpu,expl}}/t_{\text{cpu}}$	$c_{l,rms}$ (error)	$\overline{c}_d$ (error)	$c_{d,rms}$ (error)	St (error)
expl CFL = 0.5	200 000	–	1	1	1.182 (ref)	1.697 (ref)	0.192 (ref)	0.243 (ref)
IRS4 CFL = 1	100 000	5	2.09	0.5	1.181 (+0.1%)	1.696 (+0.1%)	0.192 (+0.0%)	0.242 (+0.14%)
IRS4 CFL = 2	50 000	5	2.09	1.0	1.180 (+0.1%)	1.695 (+0.2%)	0.191 (+0.1%)	0.242 (+0.25%)
IRS4 CFL = 4	25 000	5	2.09	1.9	1.179 (+0.2%)	1.694 (+0.2%)	0.191 (+0.4%)	0.242 (+0.36%)
IRS4 CFL = 8	12 500	5	2.09	3.8	1.177 (+0.4%)	1.692 (+0.3%)	0.189 (+1.1%)	0.242 (+0.41%)
IRS4 CFL = 12	8333	7	2.11	5.6	1.170 (+1.0%)	1.689 (+0.5%)	0.187 (+2.4%)	0.242 (+0.21%)
IRS4 CFL = 16	6250	10	2.43	6.5	1.157 (+2.0%)	1.684 (+0.8%)	0.181 (+5.6%)	0.244 (+0.47%)

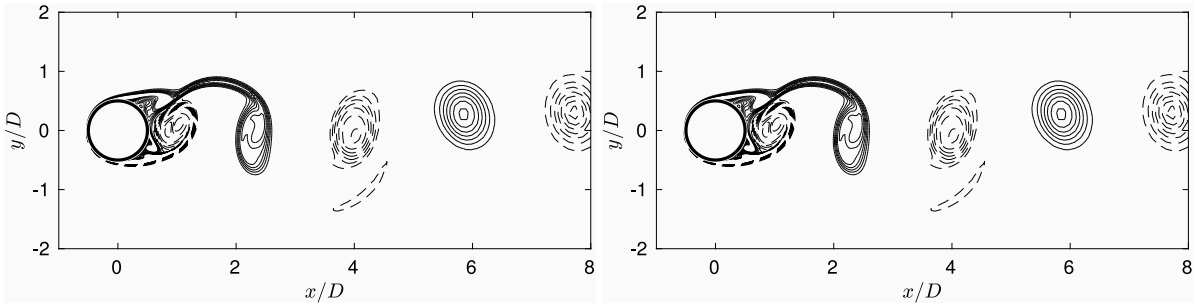

Fig. 14. Laminar flow past a cylinder at Re_D = 1200. Snapshot of the vorticity field at the same instant for the explicit at CFL = 0.5 (left) and implicit IRS4 at CFL = 16 (right). 8 positive (———) and negative (– – –) isocontours of $\omega_z D/U_\infty$ from ±1 to 8.

the cylinder starts to grow, then becomes asymmetric and a regular von Kármán vortex shedding in the wake is finally established. Starting from the same established flow solution, 7 simulations are performed over the same physical time interval using maximum CFL numbers spanning from 0.5 to 16 (see Table 3).

Close-up views of the vorticity in the cylinder wake are plotted in Fig. 14 for the two extreme CFL numbers (intermediate cases are not reported for brevity). At first glance, the vorticity field is little affected even for a time step multiplied by 32. In fact, we show below that the dispersive error of IRS4 may induce a slight shift in time. The lift coefficient history is presented in Fig. 15, and the progressive shift is visible for the two highest CFL values. Looking more closely at the last shedding cycles for lift and drag coefficients, we can see that the accumulation of phase errors is only significant for CFL_{max} 12 and 16. The quantitative errors with respect to the low-CFL explicit case are reported in Table 3. The errors for mean and fluctuating aerodynamic

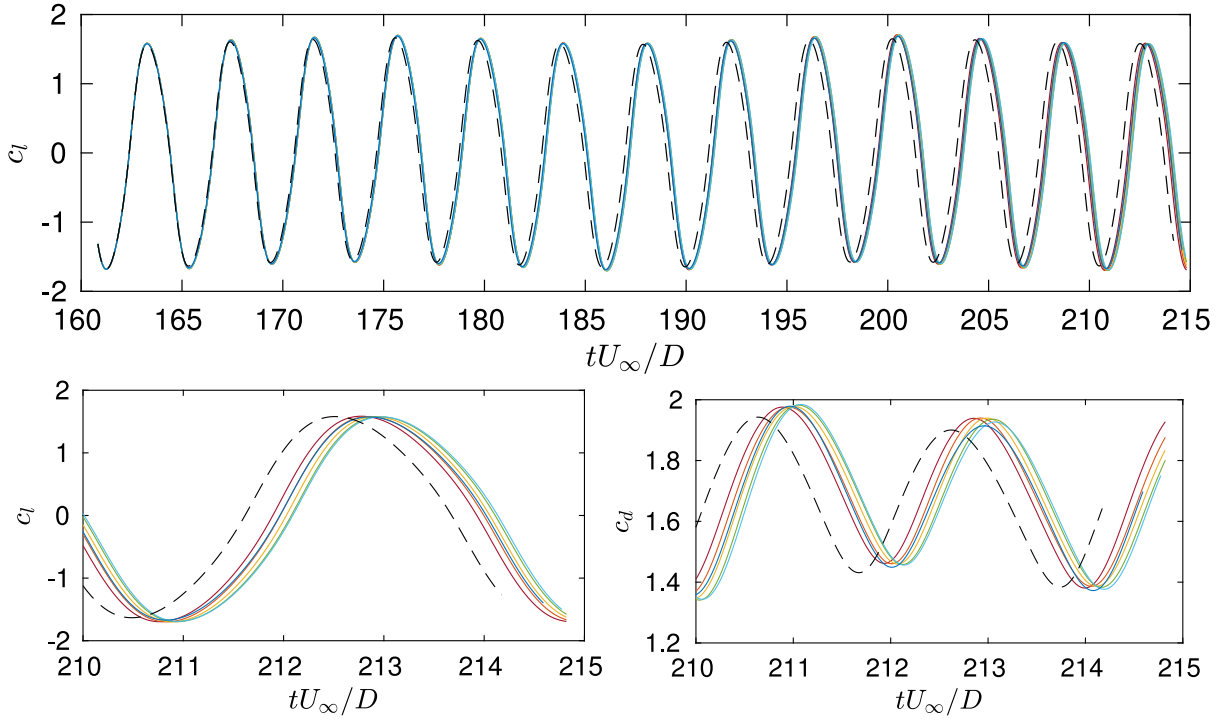

Fig. 15. Laminar flow past a cylinder at $Re_D = 1200$. Top, lift evolution for various CFL numbers (——, 0.5; ——, 1; ——, 2; ——, 4; ——, 8; ——, 12; – – –, 16). Bottom, close-up views for the lift and drag for the last simulated cycles.

coefficients remains low, below 2% for the lift and below 1% for the mean drag. The maximum error of 5% is obtained for the amplitude of drag fluctuations at $\text{CFL}_{max} = 16$, which is a sensitive quantity. The frequency of vortex shedding is obtained by computing power spectra of the lift over 13 cycles using an autoregressive method. The prediction of the Strouhal number appears robust with error below 0.5%. Estimation of CPU time are also given in Table 3. The overhead of IRS4 smoothing is more prominent in 2D, roughly 50% per implicited direction, leading to a total overhead of 100% (the cost of the explicit run at $\text{CFL}_{max} = 0.5$ is approximately the same as the implicit run at $\text{CFL}_{max} = 1$). This overhead is higher at $\text{CFL}_{max} = 16$, where 10 ghost cells are used in domain interfaces. The simulations were run on 8 cores (90 × 150 points/core). Overall, a saving of a factor of 5 can be achieved for this 2D test-case with a solution of comparable accuracy with our reference.

5.7. Turbulent flow past a cylinder at $Re_D = 3900$

The IRS4 method is then applied to the flow past a circular cylinder at $Re_D = 3900$ based on the diameter D, and at $M = 0.3$, which is a common benchmark case for curvilinear geometries [63,64]. The simulation is performed on a multi-block H-O-H grid topology with approximatively 10 millions points parallelized on 102 processors. 270 points are used around the cylinder with a first mesh size of $0.002{\times}D$, 96 points are used in the spanwise direction to discretize $2D$ and the wake extent is discretized by 405 points. Non-reflecting Tam & Dong's conditions are applied at free boundaries and a sponge zone is added at the outlet boundary. An explicit simulation is started from the initial field described in the AS1 benchmark case [64] during 500 000 iterations with a nondimensional time step $\Delta t U_\infty/D = 4.55 \times 10^{-4}$. The explicit calculation is then run for 500 000 and statistics are accumulated. Afterwards, three implicit simulations with IRS4 are run by multiplying the time step by 2, 3, 4 and dividing the number of iterations by the same amount. The IRS4 smoothing is applied in the ξ and η-directions; the number of ghost cells in MPI interfaces is ngh = 5.

The distributions of the pressure coefficient, $C_p = (\bar{p}-p_\infty)/(\frac{1}{2}\rho_\infty U_\infty^2)$, are superimposed for the explicit and implicit simulations in Fig. 16 (left). The evolution of the mean velocity along the wake centerline, in Fig. 16 (right), gives a good idea about the flow topology. In particular, the zero-crossing yields the mean recirculation length. The same values are obtained for both LES-expl and LES-IRS4 in good agreement with the measurements of Parnaudeau et al. [63]. The older experiments of Lourenco and Shih [66] gave a significantly shorter bubble. In fact, for $Re_D = 3900$, the cylinder flow corresponds to the shear-layer instability regime, where the transition to turbulence occurs in the separated shear layers [67]. This regime is characterized by a great sensitivity of the recirculation length to details of flow conditions, or numerical parameters for simulations [68,69]. For instance, Lehmkuhl et al. [68] performed simulations over a very long time and showed some intermittency between short- and long-bubble flow topologies. In the present study, the long-bubble regime is captured but it remains highly dependent on numerical setup.

The spanwise vorticity in the mid-plane in Fig. 17 (left) highlights the instabilities in the two shear layers. At the particular instant shown in the pictures, the top shear layer becomes unstable and rolls up to form a primary vortex near the end of the recirculating region. A small vortex resulting from the shear-layer instability is visible near the end of the bottom shear layer. The alternate vortex shedding from the two shear layers then forms the von Kármán street. The shedding frequency can be estimated from normal velocity spectra along the wake centerline. The spectra at $x/D = 3$ for the present explicit and implicit simulations are compared in Fig. 17 (right) with the experimental and numerical results from Parnaudeau et al. [63]. Power spectral densities are estimated with an autoregressive method for 6 shedding cycles. The velocity signal is recorded every 50 iterations for the explicit case and every 10 iterations for IRS4 cases, yielding a sampling frequency $f_s D/U_\infty$ of 44, 110, 73 and 55 for Δt, $2\Delta t$, $3\Delta t$ and $4\Delta t$, respectively. The corresponding frequency resolution is 0.0044, 0.0055, 0.0044 and 0.0044, and the peak Strouhal number 0.207, 0.209, 0.207 and 0.207 for the increasing timesteps, in good agreement with the experimental value, $St = 0.208$. Time-averaged fields, computed over the same physical duration, are shown in Fig. 18. The explicit and the implicit case

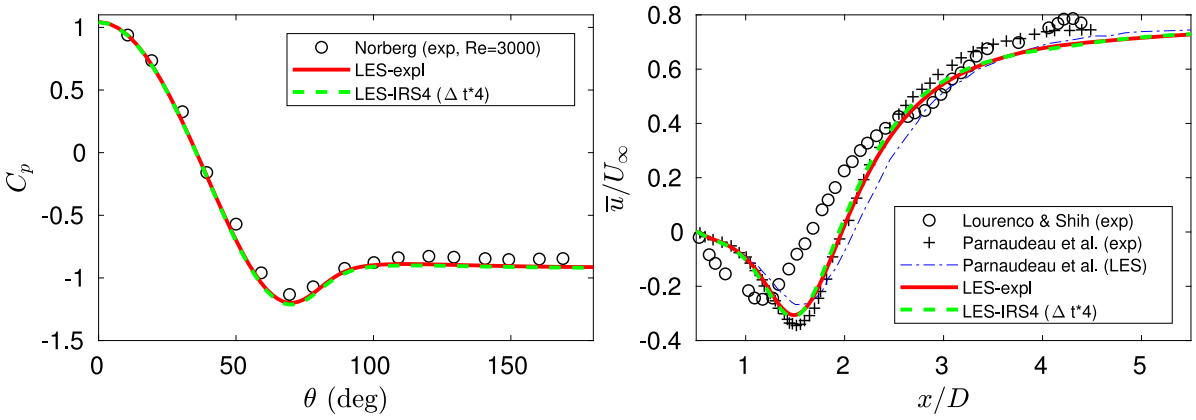

Fig. 16. Flow past a cylinder at $Re_D = 3900$: pressure coefficient on cylinder wall, compared to Norberg's experiments [65] (left), and evolution of mean streamwise velocity along the wake centerline (right), compared to experiments of Lourenco and Shih [66] and Parnaudeau et al. [63].

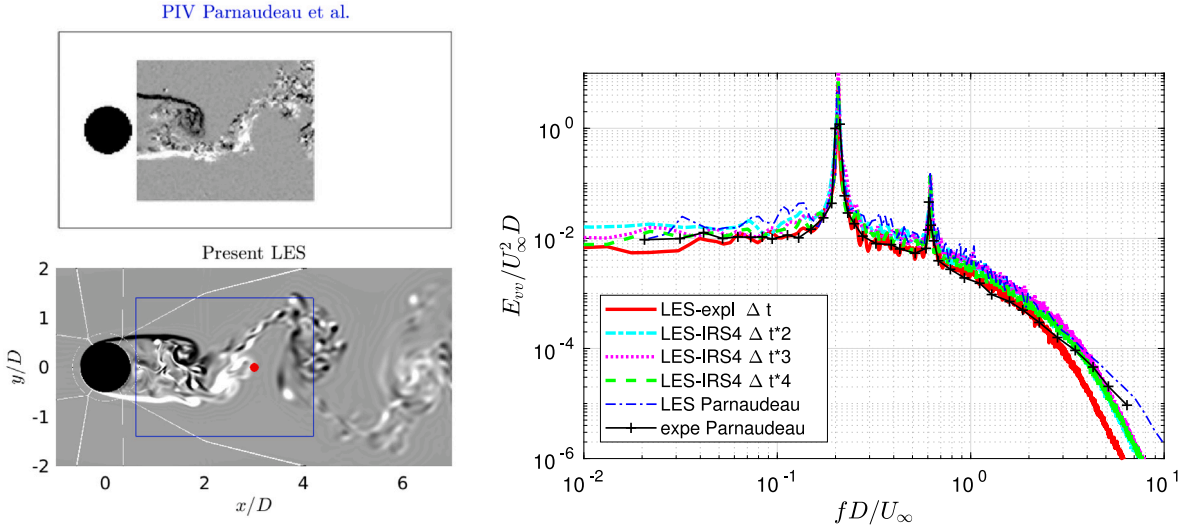

Fig. 17. Flow past a cylinder at $Re_D = 3900$: map of the spanwise vorticity $\omega_z D/U_\infty$ compared to PIV measurements of Parnaudeau et al. [63] on the left, and power spectra of the normal velocity fluctuations at the location $(x, y) = (3D, 0)$ (marked by a red point in the vorticity snapshot).

with $4\Delta t$ are almost superimposed and in very good agreement with the experiments. The overhead introduced by IRS4 is approximately 20% per direction, leading to overall savings in CPU time, due to the increased CFL, of 1.44, 2.16 and 2.98, respectively.

5.8. Laminar flow past a sphere

An example of a 3-D curvilinear multiblock mesh arrangement is the flow past a sphere at low Reynolds numbers. This flow has been largely studied in literature (e.g. [70–72]) by solving the incompressible Navier–Stokes equations. The present test case considers laminar flow over a sphere at Mach number of 0.3 and Reynolds numbers comprised between $Re_D = 50$ and 300, based on the sphere diameter D. Nagata et al. [72] have studied subsonic to supersonic flows past a sphere for the same range of Re_D. Their lowest Mach number is 0.3, so that a direct comparison is possible. The cited examples used a O-O-type grid, that is to say spherical coordinates. We are using a multiblock grid where the sphere surface is divided into six faces. For simulations at $Re_D = 50$, 100, 150 and 200, where a steady flow is expected, the outer boundary is a sphere located at $13D$ and the six blocks are identical with $50 \times 50 \times 100$ points. The last dimension is along the radial direction, where the points are clustered near the sphere wall, with a minimal mesh size of $0.012D$. In order to cluster grid points in the wake region for the unsteady case at $Re_D = 300$, we used a finer grid, with $100 \times 100 \times 200$ points in each block, and the outer boundary is an ellipsoid (see Fig. 19), as in [73]. The most upstream point is at $-10D$, the most downstream at $30D$ and the minimal mesh size is $0.008D$. Adiabatic conditions are applied at the wall and non-reflecting Tam & Dong's conditions are used at the outer boundary. Since the geometry is three-dimensional, the IRS4 is activated in all directions. We consider CFL numbers, based on minimal mesh size and velocity $U_\infty + c_\infty$, between 0.5 and 7.

Let us first discuss results for the cases at $Re_D = 50$, 100, 150 and 200. At these conditions, a steady state solution should be formed with a large toroidal vortex formed just aft of the sphere. We can evaluate the quality of the solutions by comparing the drag coefficient and the length of the recirculation region with previous published DNS and experiments. Fig. 20 presents the evolution of the drag $\overline{C}_d$ and of the recirculation length $\overline{L}/D$ as a function of the Reynolds number. At the first glance, for each Re_D, the present results for different CFL numbers are all superimposed and in very good agreement with references.

More details are given in Table 4, where errors in percentage with respect to the DNS solution of Johnson & Patel [70] are also given. The variations for $\overline{C}_d$ and $\overline{L}/D$ by varying the CFL number are indeed negligible. In the table, we also give the parameters and timing of IRS4 scheme, together with the effective maximum values

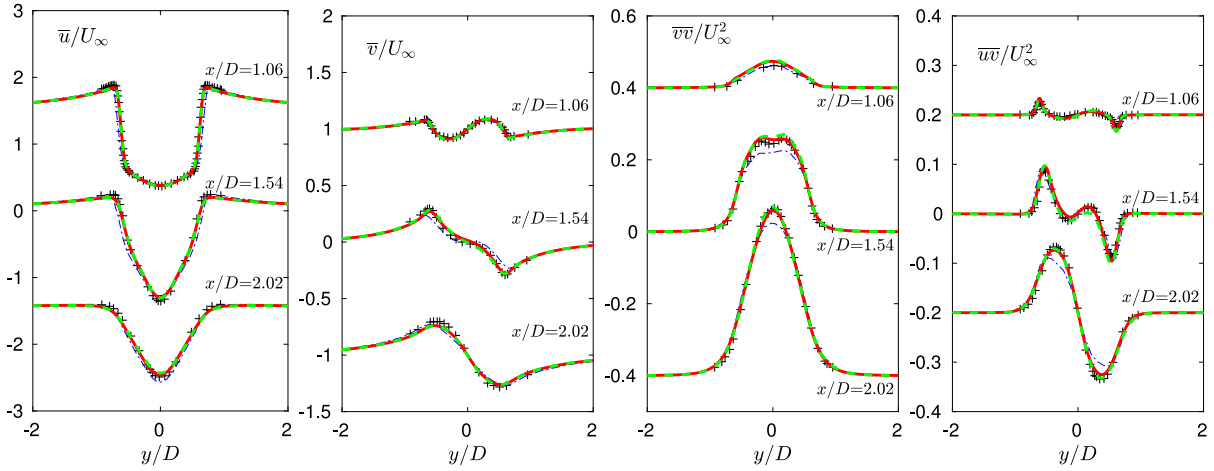

Fig. 18. Flow past a cylinder at $Re_D = 3900$: mean velocity and turbulent intensities profiles for the explicit (——) and implicit IRS4 (– – –) LES, compared to experiment (++) and LES (– · – · –) of Parnaudeau et al. [63].

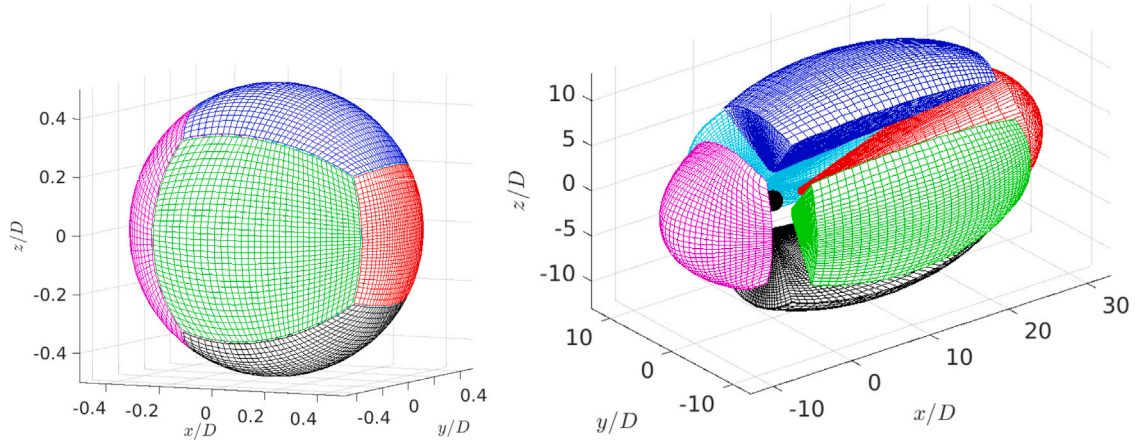

Fig. 19. Flow past a sphere at $Re_D = 300$: grid arrangement (1 every 3 points is shown). Mesh on the sphere (left) and exploded six-block grid topology (right).

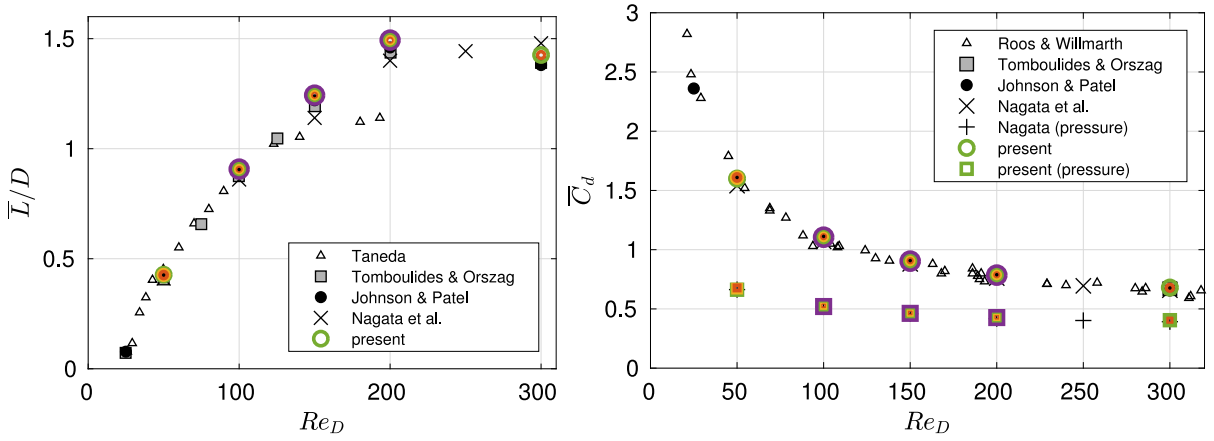

Fig. 20. Laminar flow past a sphere: recirculation length (left) and drag coefficient (right) as a function of the Reynolds number. Comparison with experiments of Taneda [74] and Roos & Willmarth [75]; incompressible DNS of Johnson & Patel [70] and Tomboulides & Orszag [71]; compressible DNS of Nagata et al. [72]. The color and size of the circles for the present simulations correspond to various CFL numbers, see Table 4.

of the CFL and Fourier criteria (the latter being denoted FC). We have proceeded as follows. An explicit simulation is performed to find the maximum CFL ensuring convergence (by increment of 0.1). The simulation is converged when all residuals decrease by at least 8 orders of magnitude. The explicit case is then taken as reference for the timing estimation. For higher CFL, IRS4 is activated and the number of ghost cells (ngh) is automatically chosen from the maximum CFL numbers in all boundaries between blocks or MPI subdomains. Note that all calculations used 96 cores, so that each MPI domain has 25^3 points. This number of points per direction is small (at the limit of scalability of the code) and has a strong impact on the overhead of IRS4 scheme per iteration. Indeed, for ngh = 12 (at CFL = 7), the number of points

Table 4
Steady laminar flow past a sphere: Stability considerations (CFL and Fourier criterion FC); parameters of IRS4 scheme (ghost cells for parallelization ngh and smoothing coefficient θ_4); timing (using explicit case as a reference); flow parameters (drag $\overline{C}_d$ and recirculation length $\overline{L}/D$) with percentage errors in parentheses with respect to DNS [70].

Case		CFL_{max}	FC_{max}	ngh	θ_4	Time/it	$t_{cpu,expl}/t_{cpu}$	$\overline{C}_d$ (error)	$\overline{L}/D$ (error)
Re50 CFL = 0.4		0.33	0.29	expl	–	1	1	1.610 (+1.9%)	0.426 (+1.4%)
Re50 CFL = 2		1.67	1.45	5	0.02	1.82	2.7	1.607 (+1.7%)	0.427 (+1.6%)
Re50 CFL = 5		4.17	3.63	9	0.01	2.38	5.3	1.600 (+1.3%)	0.428 (+1.8%)
Re100 CFL = 0.5		0.42	0.18	expl	–	1	1	1.112 (+2.0%)	0.905 (+1.7%)
Re100 CFL = 3		2.50	1.09	5	0.01	1.82	3.3	1.110 (+1.8%)	0.906 (+1.8%)
Re100 CFL = 5		4.17	1.81	9	0.0025	2.38	4.2	1.108 (+1.6%)	0.907 (+1.9%)
Re100 CFL = 7		5.84	2.54	12	0.0025	2.67	5.3	1.105 (+1.4%)	0.908 (+2.0%)
Re150 CFL = 0.5		0.42	0.12	expl	–	1	1	0.908 (+0.9%)	1.242 (+1.8%)
Re150 CFL = 3		2.50	0.73	5	0.005	–	–	0.906 (+0.7%)	1.243 (+1.9%)
Re150 CFL = 5		4.17	1.21	9	0.0025	2.35	4.2	0.905 (+0.6%)	1.243 (+1.9%)
Re150 CFL = 7		5.84	1.69	12	0.0025	2.67	5.3	0.903 (+0.4%)	1.243 (+1.9%)
Re200 CFL = 0.7		0.58	0.13	expl	–	1	1	0.789 (+1.1%)	1.492 (+2.2%)
Re200 CFL = 3		2.50	0.54	5	0.0025	1.82	2.4	0.788 (+1.0%)	1.493 (+2.3%)
Re200 CFL = 5		4.17	0.91	9	0.0025	2.30	3.1	0.787 (+0.8%)	1.493 (+2.3%)
Re200 CFL = 7		5.84	1.27	12	0.0025	2.60	3.9	0.785 (+0.7%)	1.493 (+2.3%)

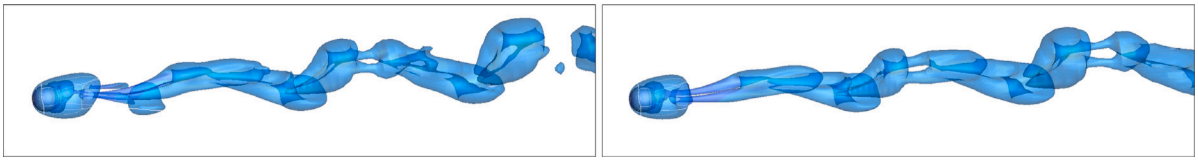

Fig. 21. Laminar flow past a sphere at $Re_D = 300$: instantaneous isocontour of Q-criterion ($Q = 10^{-3}U_\infty^2/D^2$) for EXPL (left) and IRS4 (right) simulations.

per direction is 12 + 25 + 12, say the double, explaining the rapid increase of time/it as the CFL (thus ngh) is higher. That being said, the acceleration factor, measured as the ratio with the CPU time for the explicit case, remains between 3 and 5. The last remark is about the value of the smoothing parameter θ_4 for IRS4. Since we are considering very low Reynolds number, the most limiting criterion can be the viscous stability condition, which imposes the Fourier criterion FC to be lower than 0.696 for the considered RK4 scheme. It is more rapidly violated as Re_D is lower, jeopardizing the convergence, especially for CFL numbers around 2 and 3 (where we have a peak in the scheme instability). In the present implementation, we did not take the viscous stability into account and the convergence is obtained by increasing θ_4 (up to 0.02, 8 times the nominal value deduced from the stability study for the advection equation). This is not detrimental for the accuracy since a steady solution is found, which does not depend on the accuracy of the time advancement scheme. If one wants to perform unsteady simulations with high Fourier criteria (fine grids with low Reynolds numbers), it is possible to modify the definition of the spectral radius, adding a condition on the diffusion spectral radius $\gamma\mu/\rho Pr$ with respect to the Fourier criterion (see [76]). In summary, this first series of simulations does not constitute a favorable test-case, nor in terms of stability since the viscous stability becomes dominant and the grid is relatively uniform (meaning that large values of CFL and FC are obtained on an extended region), nor in terms of computing time since a small number of points per direction in MPI domains is used. The time savings using IRS4 are notwithstanding significant.

To further demonstrate that IRS4 preserves time accuracy, we now consider $Re_D = 300$ on the finer grid, shown in Fig. 19. The explicit simulation is carried out for CFL = 0.5 and the implicit one for CFL = 4 (increase by a factor of 8 of the timestep), with nominal values of IRS4 smoothing coefficients and ngh = 10. For the implicit case, the effective maximal values for CFL and Fourier criterion FC are 4.81 and 1.19, respectively. Instantaneous snapshots of the vortical structures in Fig. 21 show similar flow fields for the two computations. The asymmetric vortex shedding forms hairpin structures convected in the wake, in good qualitative and quantitative agreement with DNS [70,71] and dye visualizations [70,77]. A Fourier analysis of drag signal gives a Strouhal number for the vortex shedding of 0.131, in agreement with previous findings (see Table 5). The shedding frequency is slightly lower than incompressible DNS but very close to the compressible simulation [72] at the same Mach number.

The mean and rms streamwise velocity along the wake centerline are plotted in Fig. 22. The zero-crossing of $\overline{u}$ yields the recirculation length $\overline{L}/D$, which is in good agreement with references in Table 5, in between the incompressible [70,71] and compressible [72] DNS. A slightly shorter bubble is obtained for the large-timestep IRS4 case. The averaged fluctuating velocity profiles are almost superimposed with results of [70,71] in Fig. 22 (right), demonstrating the good accuracy of IRS4 in a fully three-dimensional unsteady application. The simulations have been run on 768 cores (25^3 points/MPI domain) and give a CPU time per iteration increased by a factor 2.3 for IRS4. This is coherent with lower Reynolds cases since ngh = 10 and small MPI domains are considered. The resulting acceleration factor for implicit case is 3.5, that is to say the same physical time is reached 3.5 faster.

5.9. Turbulent flow past a sphere at $Re_D = 3700$

The flow past a sphere at $Re_D = 3700$ is a canonical flow over a three-dimensional body, which presents challenges common to accurate computation over bluff bodies at moderate Reynolds numbers: a thin laminar boundary layer, flow separation at a location not known a priori, transition to turbulence in thin shear layers, followed by an unsteady turbulent wake. The computation of the turbulent flow over a sphere at $Re_D = 3700$ has been carried by LES [79] and DNS [80–82]. The incompressible Navier–Stokes equations are solved on unstructured grids in [80,81] or using an immersed boundary method [79,82]. In the present study, a complex structured multiblock mesh (see Fig. 23) is used to demonstrate the effectiveness of the proposed multidomain approach for the IRS4 implicit time advancement. Furthermore, the compressible Navier–Stokes equations are solved. We set a Mach number $M = 0.3$, so that a comparison with previous work is possible. An example of compressible flow simulations is the recent study by Nagata et al. [83], who considered Mach numbers between 0.3 and 2 at Reynolds numbers up to 1000.

The grid arrangement, shown in Fig. 23, consists in 16 blocks. A 6-block O-topology is used around the sphere up to a radius of $1.2D$,

Table 5
Flow past a sphere at $Re_D = 300$: Comparison of statistical flow quantities with previous experimental and computational results.

	$\overline{C}_d$	$\overline{C}_{d,p}$	$C_{d,rms}$	$\overline{C}_l$	$C_{l,rms}$	St_w	$\overline{L}/D$
Present EXPL (CFL = 0.5)	0.675	0.402	2.1×10^{-3}	−0.043	0.0066	0.131	1.44
Present IRS4 (CFL = 4)	0.675	0.401	2.1×10^{-3}	−0.036	0.0062	0.131	1.426
Johnson & Patel [70]	0.656		3.5×10^{-3}	−0.069	0.016	0.137	1.38
Tomboulides & Orszag [71]	0.671		2.8×10^{-3}			0.136	1.39
Nagata et al. [72]	0.658	0.392			0.010	0.130	1.48
Roos & Willmarth [75] (exp)	0.629						
Sakamoto & Haniu [78] (exp)						0.15–0.165	

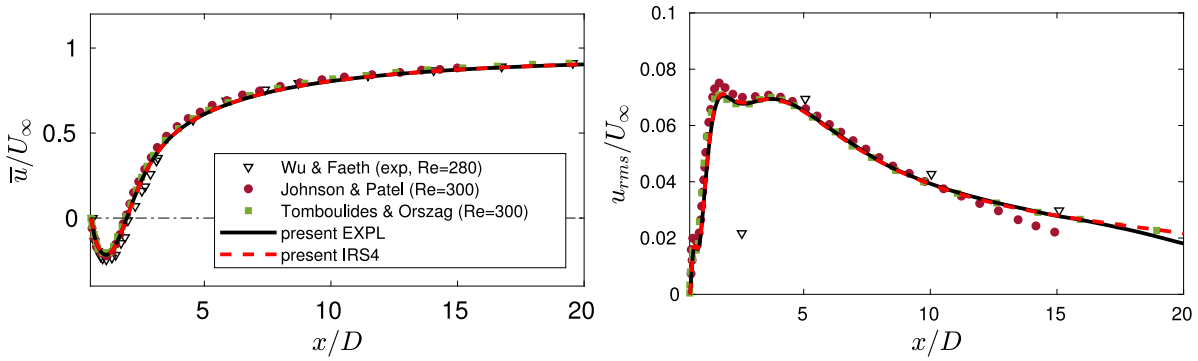

Fig. 22. Flow past a sphere at $Re_D = 300$: mean streamwise velocity (left) and mean fluctuating streamwise velocity (right) profiles along the wake centerline.

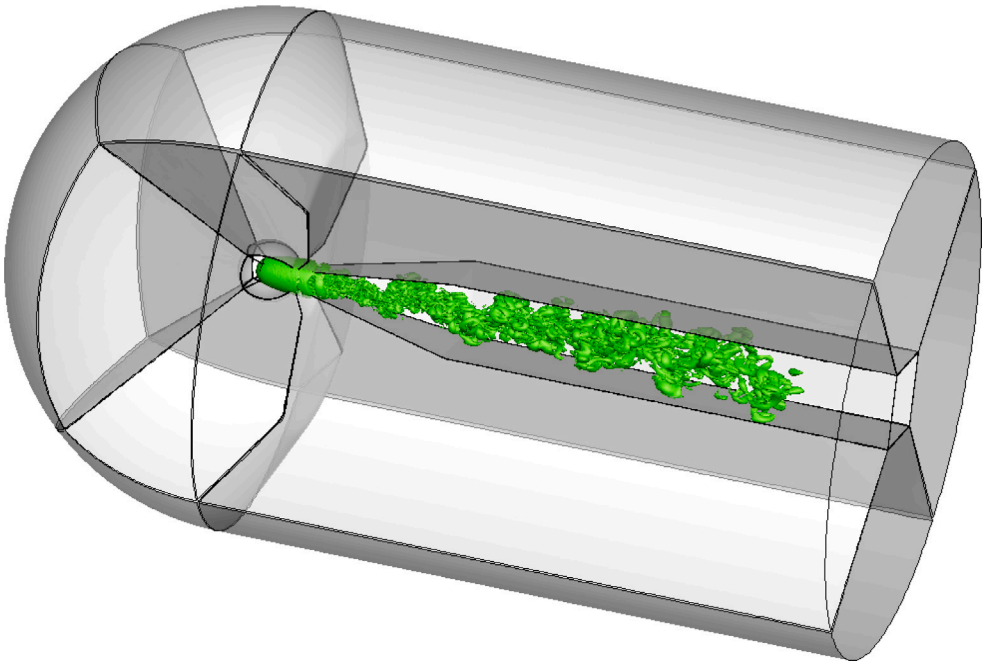

Fig. 23. Flow past a sphere at $Re_D = 3700$.

each block having 100^3 points. On the upstream side, 5 blocks with the same number of points are used to generate a hemispherical boundary up to $10D$. The dowstream part has a cylindrical outer boundary of radius $10D$ and extends up to $25D$ in the streamwise direction with 350 points, so that the wake is discretized by 450 points. The total number of points is 28,5 millions which is cut in subdomains of 50^3 (228 proc.) or 25^3 (1824 proc.). Based on the minimal mesh size at the wall of $0.002D$ and the maximal velocity $U_\infty + c_\infty$, where U_∞ denotes the freestream velocity of 103.8 m/s, the CFL number for the simulation using explicit time advancement (referred to as EXPL) is 0.7. A second simulation with the IRS4 is run with CFL = 5.6, *i.e.* 8 times larger. Since the geometry is three-dimensional, the smoothing is applied in the three directions ξ, η and ζ. At CFL = 5.6, 6 ghost cells are used for the multidomain application of IRS4. Fig. 24 shows the vortex structures for the two simulations. The shedding of large-scale vortices at random azimuthal positions in the shear layer gives rise to a helical-like wake. A spectral analysis of velocity signals (no shown for brevity) yields two main frequencies as expected [78,84]. The higher frequency, dominant in the shear layers (e.g. at $x/D = 1$ and $y/D = 0.6$), represents the shear layer instability. It corresponds to Strouhal numbers $St_{KH} = fD/U_\infty \simeq 0.89$ for both EXPL and IRS4 simulations. The lower frequency (dominant at $x/D = 3$ and $y/D = 0.5$) corresponds to the wake instability. We obtain $St_w = 0.215$ and 0.218 for the two simulations, in very good agreement with previous experimental and computational results (see Table 6).

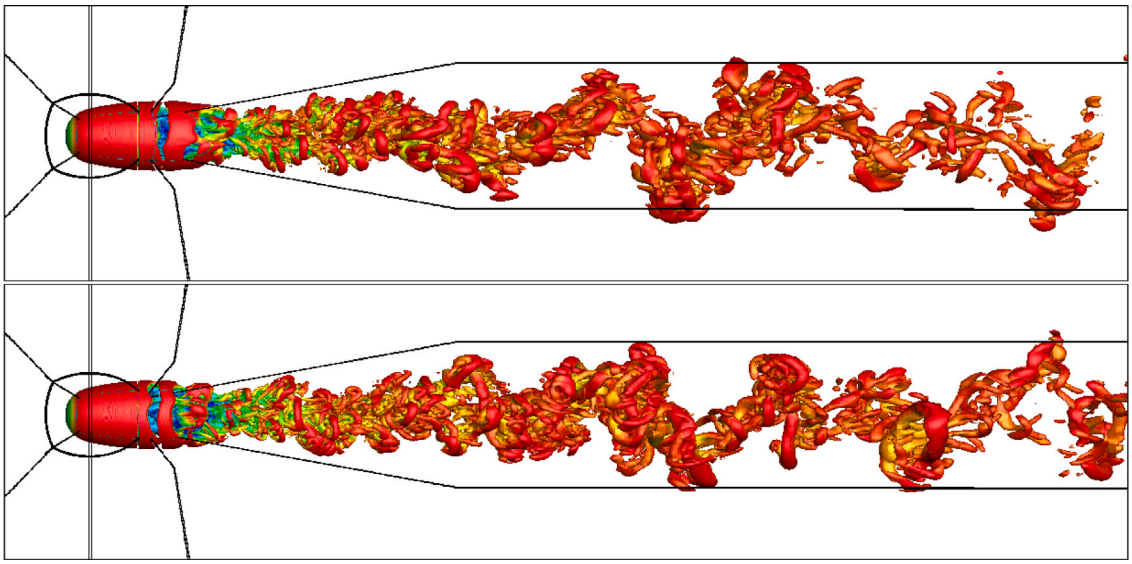

Fig. 24. Flow past a sphere at $Re_D = 3700$: side view of Q-criterion for EXPL (top) and IRS4 (bottom) simulations (isocontour Q = $0.1U_\infty^2/D^2$ colored by streamwise velocity with blue to red levels between −0.2 and $1U_\infty$).

Table 6
Comparison of statistical flow quantities with previous experimental and computational results.

	$\overline{C}_d$	$\overline{C}_{pb}$	St_w	θ_{sep} (deg)	$\overline{L}/D$
Present EXPL (LES)	0.390	−0.208	0.215	90	2.55
Present IRS4 (LES)	0.394	−0.213	0.218	90	2.42
Schlichting [85] (exp)	0.39				
Kim & Durbin [84] (exp)		−0.224	0.22		
Sakamoto & Haniu [78] (exp)			0.21		
Yun et al. [79] (LES)	0.355	−0.194	0.21	90	2.62
Rodriguez et al. [80] (DNS)	0.394	−0.207	0.215	89.4	2.28
Bazilevs et al. [81] (DNS)	0.392	−0.207	0.221	89.4	2.28
Li et al. [82] (DNS)	0.385	–	0.218	89	2.3

Time histories of the drag C_d coefficients are reported in Fig. 25, which do not show the frequency components corresponding to the shear-layer and wake instabilities. This is because strong large-scale modulations are dominating the signals. Similar results are reported in the literature and the values of the mean drag coefficients are in good agreement with experiments and incompressible simulations (Table 6). The pressure distribution along the sphere wall at $z = 0$, shown in Fig. 26 (left), matches the previous DNS. The value of the stagnation pressure is slightly greater than one due to the Mach number of 0.3. The skin friction is used to determine the mean separation angle θ_{sep}, which allows in turn to compute the back-pressure coefficients C_{pb}. The values of θ_{sep} and C_{pb} reported in Table 6 are also in good agreement between the explicit and implicit simulations, and with respect to literature results.

First- and second-order statistics are computed over the last 400 time units and are reported in Figs. 26 and 27. The zero-crossing of the axial velocity in Fig. 27 (left) gives the mean recirculation length. The values $\overline{L}/D = 2.58$ and 2.47 are slightly higher than the values ∼2.3 obtained in the DNS of [80–82]. This quantity is highly sensitive to the resolution for a cylinder in shear-layer transition regime, as discussed in Section 5.7. For a sphere, it is less critical but some variations are observed. For instance the well-resolved LES of Yun et al. [79] gave a value of 2.62. The longer length of the recirculation zone will impact the comparison of mean and fluctuating velocity profiles. Vertical profiles for the three stations $x/D = 0.2$, 1.6 and 3, for which experimental results are available, are reported in Fig. 26 (right). Above the sphere and in the near wake, all the profiles almost collapse, whereas a greater sensitivity is observed at $x/D = 3$, since the recovery flow after the recirculation is more or less achieved. The experimental Ref. [84] would indicate a smaller bubble, but the latter can depend on the level of freestream disturbances. Some studies [81] show that freestream turbulence dramatically reduces the length of the recirculation region. The turbulent intensities are very similar for the two simulations and the incompressible DNS [80]. The streamwise evolution of u_{rms} is reported in Fig. 27 (right) and some vertical profiles at several stations in the wake are compared in Fig. 28. Some discrepancies between implicit and explicit, or with respect to incompressible DNS of Rodriguez et al. [80] are difficult to interpret. Bazilevs et al. [81] compared the same profiles averaged on three different time windows and showed a variability of the same order of magnitude as the present deviations.

Overall, we can conclude that the quality of the results for the calculations at CFL = 0.7 and 5.6 are very similar. Strictly speaking, the IRS4 statistical parameters are even slightly closer to the reference DNS. In terms of computing time, the simulations have been run on 228 or 1824 cores (50^3 and 25^3 points/MPI domain, respectively). The time per iteration for IRS4 is increased by a factor of approximately 2 and 1.6, respectively. The number of ghost cells for parallelization is 5 and we can measure the effect of dividing in smaller MPI subdomains on the computing time. For 50^3 points per domain, we obtain again an overhead of 20% per implicited direction and the acceleration factor is 5 with respect to the explicit case.

5.10. LES of internal flow in a fluidic actuator

The last example represents a complex geometry, namely the simulation of the internal flow inside a fluidic actuator and the pulsed jets exiting in the free-field. The principle of the pulsed-jet actuator (PJA) is based solely on fluid dynamic phenomena with no moving parts. The alternate pulsed jets, exiting in the free field (see Fig. 29), are generated by the periodic oscillations of the compressible internal jet, which attaches alternatively on left and right walls due to Coanda effect in response to pressure differences established in the feedback loops. The incoming jet is supplied by a pressure difference between the pressurized air with total pressure of 1.5 bar at inlet and the atmospheric pressure. Before entering the interaction region of the actuator (see Fig. 29), the jet reaches a Mach number of 0.75 at the nozzle throat which makes the flow field subsonic but highly compressible in the interaction region. It is worth noting that this small region includes a large range of turbulent structures, from the most energetic scales to

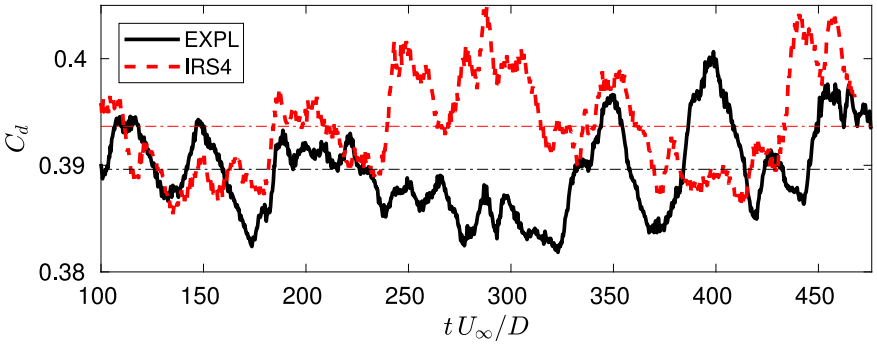

Fig. 25. Flow past a sphere at $Re_D = 3700$: Time histories of the drag coefficients (dash-dotted lines indicate mean values).

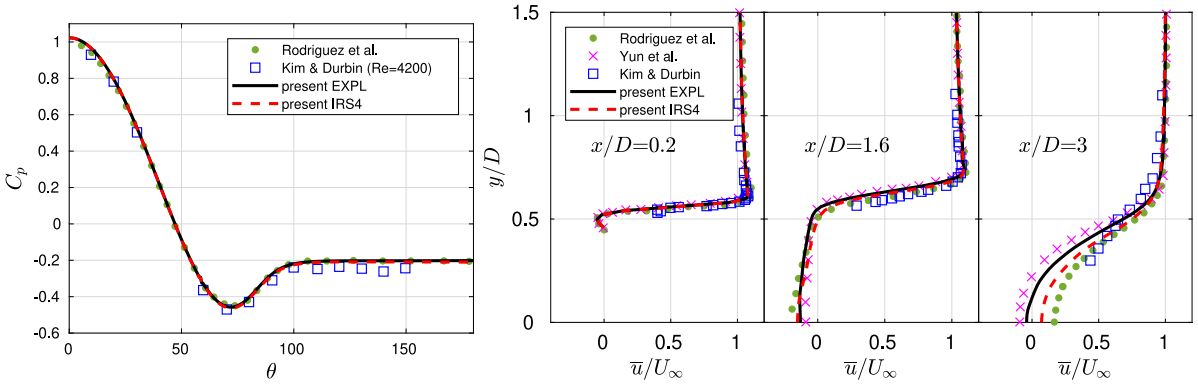

Fig. 26. Flow past a sphere at $Re_D = 3700$: pressure coefficient distribution as a function of the angular position, on the left, and mean streamwise velocity profiles at three streamwise stations, on the right.

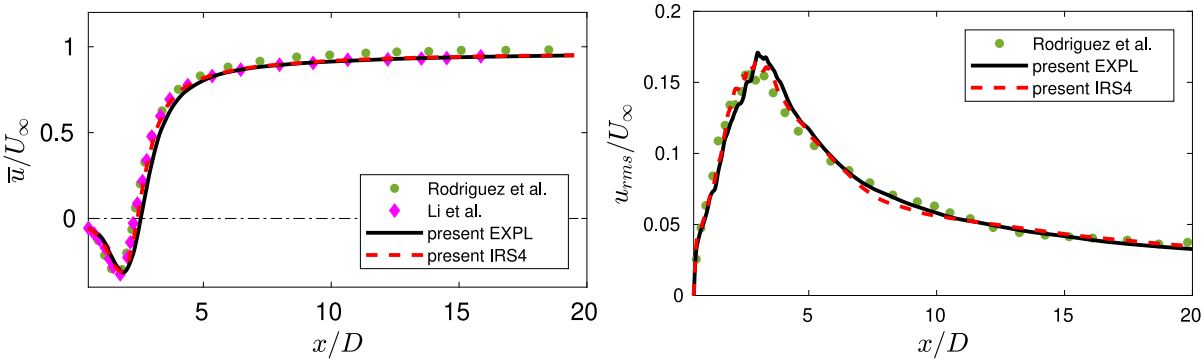

Fig. 27. Flow past a sphere at $Re_D = 3700$: mean streamwise velocity (left) and mean fluctuating streamwise velocity (right) profiles along the wake centerline.

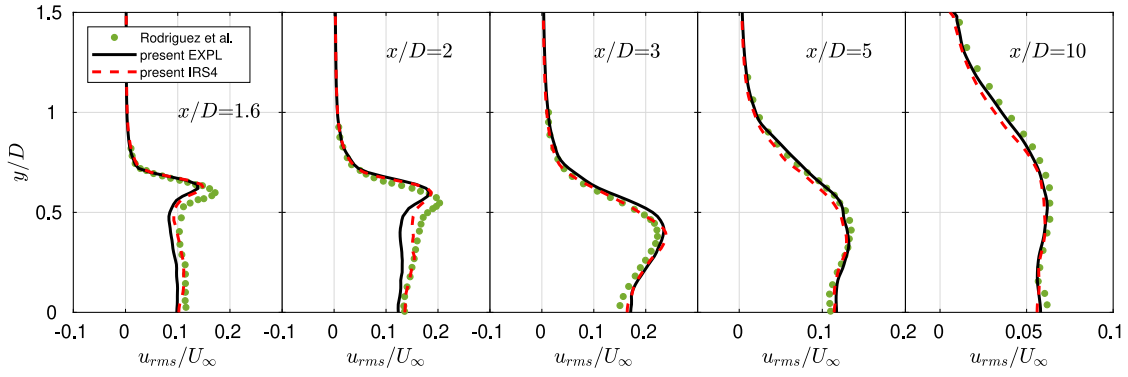

Fig. 28. Flow past a sphere at $Re_D = 3700$: mean streamwise fluctuating velocity profiles along vertical lines at x/D = 1.6, 2, 3, 5 and 10.

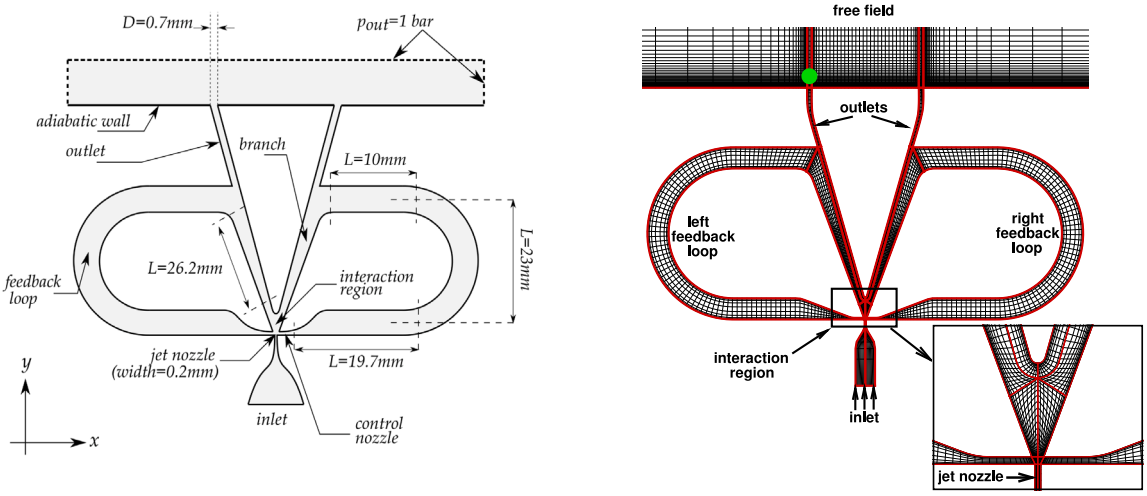

Fig. 29. Internal flow in a fluidic actuator: illustration of the PJA including dimensions and boundary conditions (left) and 2D view of the computational domain of the fluidic actuator with a close-up view of the interaction region (right).

the smallest ones. The simulation is carried out using the same wall-resolved LES strategy as the previous problems. The computational domain shown in Fig. 29 consists of 19 blocks having a structured curvilinear grid topology. Due to the complexity of the domain, 5 blocks share the same corner grid node, which locates in the vicinity of the center of the interaction region. This makes the problem a challenging case to test the multiblock implementation of IRS4. Each block is meshed using the resolution of $\Delta x^+ = 30$ in the streamwise direction, $\Delta y_w^+ = 1$ at the wall in the wall-normal direction, and $\Delta z^+ = 15$ in the spanwise direction where 30 grid nodes are uniformly distributed. The grid stretching ratio is limited to 1.07 inside the actuator. The whole domain includes approximately 30 million grid nodes. At the inlet boundary, a subsonic boundary condition based on Riemann invariants is applied to specify the total pressure value as 1.5 bar. At the free boundaries, non-reflecting Tam & Dong's conditions are imposed. All the remaining boundaries are treated by no-slip adiabatic conditions, and periodicity is set in the spanwise direction.

The parallel simulation is performed by 1000 processors. The initial transient phase is run using the explicit time integration which limits CFL_{max} to 0.4 in this problem. Then, the time integration is switched to IRS4, which allows to increase CFL_{max} to 3.0. Note that the number of ghost points is automatically set to ngh = 2 CFL_{max} + 1 = 7 in all interfaces. The IRS4 smoothing is applied in the ξ and η-directions, which causes a computational overhead of 70% in total. Hence, a CPU saving time of 4.4 is obtained. The LES with IRS4 is run for 2 400 000 iterations, corresponding to 15 oscillation periods.

Fig. 30 shows instantaneous views of the flowfield in the interaction region, with 2D Mach contours with streamlines on the left and a 3D isocontour of the vorticity magnitude at the same instant on the right. The jet is partially attached on the left wall during its switching from right to left. It is observed that, although the attached part is almost 2D, the complex interaction with the oscillating jet is highly unsteady and 3D involving various recirculation regions as well as different scales of structures.

The present PJA configuration has been studied experimentally in [86], with the same dimensions and pressure supply. Fig. 31(left) shows a comparison of the exit velocity magnitudes with hot-wire measurements of [86], at the green point shown in Fig. 29. LES-IRS4 results are in good agreement with the measured data. The Fourier transform of the velocity signal is shown in Fig. 31(right), where the agreement is good up to the hot-wire cut-off frequency. The wall-resolved LES allows to extend the high frequency range of one decade in the inertial turbulence. The dynamics of the pulsed jet, which directly affect the exit velocity profile, are well predicted by the current strategy. More details can be found in [87]. Overall, it can be said that the IRS4 scheme works efficiently in this kind of complex geometry with a challenging multiblock arrangement.

6. Conclusion

A fourth-order-accurate implicit residual smoothing (IRS4) operator is used for time implicitation of a compressible Navier–Stokes solver on multi-block curvilinear meshes. The solver makes use of high-order finite-difference schemes supplemented with selective explicit filtering or artificial dissipation. The IRS4 operator acts as an implicit filter on the solution increments at each substep of the underlying Runge–Kutta algorithm. It modifies the spectral properties of the spatial operator and essentially introduces a dispersive error by contracting the locus of the spatial operator near the imaginary axis.

Several improvements were introduced with respect to the original version [4] to enhance robustness at high CFL and to enable the use of three dimensional curvilinear grids.

First, we showed that the use of a selective filtering strategy instead of the artificial viscosity improves damping of underresolved solution modes, enhancing robustness. Indeed, numerical dissipation terms in the spatial scheme tend to be contracted to zero by the IRS4 operator, which can compromise the effective removal of spurious oscillations near the grid cut-off. On the contrary, the filtering is independent of the time advance method and can be applied at the end of each time iteration to damp grid-to-grid oscillations.

Second, we introduced reduced-stencil IRS operators to fill the IRS matrix near the domain boundaries. Coefficients on the first row of the pentadiagonal matrix correspond to a one-sided IRS1 operator, and IRS2 coefficients are used for the second row. Such an approach exhibits better stability properties than simply truncating the operator matrix.

Third, we discussed the parallel and multi-block implementation of the method. The latter relies on an overlap between adjacent domains, where ghost points are communicated. An optimal overlap width is found to be of the order of 2CFL + 1, which limits the propagation of numerical errors due to matrix approximations at block boundaries to within the overlapped regions.

The IRS4 was finally reformulated in a finite-difference framework for three-dimensional curvilinear grids. Coupling of mesh directions through the coordinate transform is accounted by using the spectral radius of the inviscid flux Jacobian, averaged over all directions, as the characteristic velocity scale in the IRS4 operator.

The method was applied to a variety of flow problems, ranging from inviscid vortex advection to massively parallel DNS and LES of

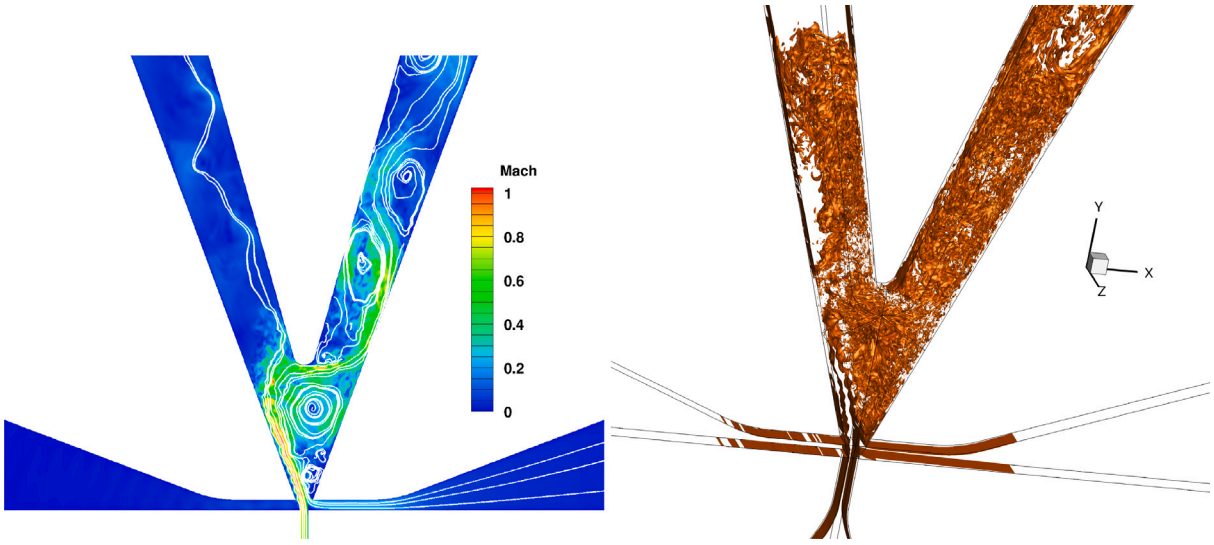

Fig. 30. Internal flow in a fluidic actuator: snapshots of Mach contours with streamlines seeded by the jet (left) and isocontour of vorticity magnitude (right).

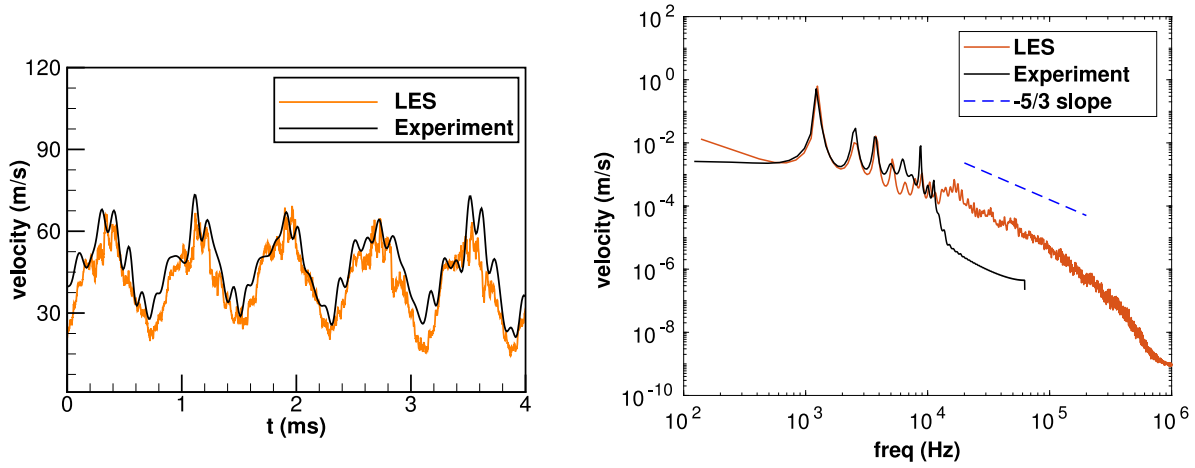

Fig. 31. Internal flow in a fluidic actuator: time history of 4 cycles of exit velocity magnitude (left) and velocity spectrum (right), at the green point shown in Fig. 29. LES-IRS4 (——) is compared to experimental data [86] (——).

turbulent flows. Computational time savings of a factor of 3 to 5 in 3D have been observed for scale-resolving turbulent simulations, despite the overhead of inverting the IRS4 matrix. The latter is found to be approximately 15 to 30% per direction. Depending on the choice of MPI subdomains, the number of ghost cells (ngh) required for IRS4 parallelization can be higher than the nominal value of 5 imposed by the discretization stencil of the spatial scheme, in order to satisfy the overlap condition of 2CFL + 1 points. This increase of ngh can result in an additional cost, especially for small subdomains. However, since computational meshes are generally clustered near the solid walls to resolve the boundary layers, the CFL values encountered in practice at MPI interfaces are rather small, making the use of a large overlap region unnecessary. Of note, for Cartesian grids, smoothing can be applied only in the wall-normal direction, so that the implicitation overhead can be greatly reduced. On curvilinear grids, due to the coupling of directions in the coordinate transform, the smoothing is activated in all curvilinear directions (2 or 3 depending on the grid topology). The overall accuracy of the turbulent scale-resolving simulations is not affected by the time implicitation, since the time step given by the CFL criterion for explicit schemes is generally significantly smaller than the minimum time step required to capture the flow physics. For very low Reynolds number and fine grids, such as the laminar flow past a sphere, the viscous stability criterion can become the most restrictive (at least when the CFL is high). In such a case, it can be necessary to increase the smoothing parameter θ_4 to restore stability, resulting in slightly higher numerical errors. Another possibility, to be explored in the future, would be to include the spectral radius of the viscous fluxes in the IRS operator.

Finally, to demonstrate the ability of the proposed methodology to provide accurate and efficient solutions of turbulent flows in a complex multi-block grid arrangement, we reported numerical results for a compressible flow inside a fluidic actuator. Further applications of the proposed method to fluidic actuators with higher pressure ratios (involving supersonic flow conditions), have been discussed in [87]. The approach has been also applied successfully to the LES of flows past transonic cylinders in [88].

Future work will further address the combination of selective filtering and low-order numerical dissipation to simulate flows with shocks. This will allow to simulate efficiently complex configurations, such as turbomachinery flows, or turbulent flows involving low-frequency oscillations, such as shock wave-boundary layer interations.

Declaration of competing interest

The authors declare the following financial interests/personal relationships which may be considered as potential competing interests: Xavier Gloerfelt reports financial support was provided by Agence National de la Recherche (ANR).

Data availability

Data will be made available on request.

Acknowledgments

This research has received funding from the Agence Nationale de la Recherche, France through the ANR-20-CE92-0019-02 project Regal-ORC and from the Clean Sky 2 Joint Undertaking (JU) under grant agreement No 887010. This work was granted access to the HPC resources of IDRIS and TGCC under the allocation A0112A01736 made by GENCI (Grand Equipement National de Calcul Intensif).

Appendix. Flow chart for implementation

Below we present a flow chart for the implementation of IRS smoothing in a Runge–Kutta time stepping algorithm. For convenience, we pose the scheme as $\mathbf{U}_t = \text{rhs}$, where

$$\text{rhs} = \underbrace{-\frac{1}{J}\left(\frac{\partial \mathbf{F}_c^e}{\partial \xi} + \frac{\partial \mathbf{G}_c^e}{\partial \eta} + \frac{\partial \mathbf{H}_c^e}{\partial \zeta}\right)}_{\text{Eulerian fluxes}} + \underbrace{\frac{1}{J}\left(\frac{\partial \mathbf{F}_c^v}{\partial \xi} + \frac{\partial \mathbf{G}_c^v}{\partial \eta} + \frac{\partial \mathbf{H}_c^v}{\partial \zeta}\right)}_{\text{viscous fluxes}}$$

First, during the initialization phase of the computer code, the number of ghost cells ngh for domain interfaces (either block or MPI subdomain) are determined and the MPI types for communications are built:

- Compute maximum CFL number in each interfaces
- Set ngh corresponding to 2CFL + 1 ghost points
- Allocate increment arrays with extended ghost points
- Define MPI types for communications

Next, we summarize the flow in the code (unplugging IRS would correspond to skip step 7. in magenta color). Loop over time and Runge–Kutta stages ($k = 1...s$) and, starting from solution $\mathbf{U}^{(n)}$ at time index n, compute the following at each stage:

1. Apply wall boundary conditions
2. Compute primitive variables (u_i, p, T)
3. Apply other boundary conditions (non-reflecting, inflow, outflow)
4. Form Eulerian fluxes
5. Compute difference approximations of Eulerian fluxes to give rhs
6. *at last RK stage only ($k = s$):*
   - Compute viscosity & thermal conductivity
   - Compute velocity & temperature gradients
   - Communicate velocity & temperature gradients
   - Form viscous fluxes
   - Compute difference approximations of viscous fluxes, added to rhs
7. Loop * on implicited direction (i, j, k): Apply implicit residual smoothing
   - If wall, do not take into account the wall points
   - Calculation of the local CFL number at index-1/2
   - Communicate CFL in implicited direction
   - Construct the pentadiagonal matrix on extended subdomain (with boundary schemes)
   - Solve the pentadiagonal linear system (Thomas' algorithm)
   - Update the solution increments: smoothed rhs

   End Loop *
8. Update conservative variables $\mathbf{U}^{(k)}(i,j,k) = \mathbf{U}^{(n)}(i,j,k) + \Delta t \alpha_k \text{rhs}(i,j,k)$
9. Communicate conservative variables (MPI)
10. *at last RK stage only ($k = s$):* numerical dissipation terms
    - Apply solution filtering
    - Apply sponge zone
    - Update conservative variables and communicate, $\mathbf{U}^{(n+1)} = \mathbf{U}^{(s)}$

References

[1] Choi H, Moin P. On the space–time characteristics of wall-pressure fluctuations. Phys Fluids A 1990;2(8):1450–60.
[2] Jameson A, Baker T. Solution of the Euler equations for complex configurations. In: AIAA paper 83-1929. 1983.
[3] Haelterman R, Vierendeels J, Van Heule D. Optimization of the Runge-Kutta iteration with residual smoothing. J Comput Appl Math 2010;234:253–71.
[4] Cinnella P, Content C. High-order implicit residual smoothing time scheme for direct and large eddy simulations of compressible flows. J Comput Phys 2016;277:72–100.
[5] Hoarau J-C, Cinnella P, Gloerfelt X. Large eddy simulation of turbomachinery flows using a high-order implicit residual smoothing scheme. Comput & Fluids 2020;198:104395—-104395–13.
[6] Lerat A. Une classe de schémas aux différences implicites pour les systèmes hyperboliques de lois de conservation. C R Acad Sci 1979;288A:1033.
[7] Lerat A, Sidès J, Daru V. An implicit finite-volume method for solving the Euler equations. In: Lecture notes in physics, vol. 170. 1982, p. 343–9.
[8] Lerat A. Implicit methods of second order accuracy for the euler equations. AIAA J 1985;23(1):33–40.
[9] Khalfallah K, Lacombe G, Lerat A. Analysis of implicit treatments for centred Euler solver. Comput & Fluids 1993;22(2/3):381–406.
[10] Martinelli L, Jameson A. Validation of a multigrid method for the Reynolds averaged equations. In: AIAA paper 88-0414. 1988.
[11] Swanson R, Turkel E, Rossow C-C. Convergence acceleration of Runge-Kutta schemes for solving the Navier-Stokes equations. J Comput Phys 2007;224:365–88.
[12] van Leer B, Tai C-H, Powell K. Design of optimally smoothing multi-stage schemes for the Euler equations. In: AIAA paper 89-1933. 1989.
[13] Jorgenson P, Chima R. An unconditionally stable Runge-Kutta method for unsteady flows. In: AIAA paper 89-0205Also NASA technical memorandum. 1989, 101347.
[14] Turkel E, Swanson R, Vatsa V, White J. Multigrid for hypersonic viscous two- and three-dimensional flows. AIAA paper 91-1572Also NASA contractor report 187603, ICASE Report No. 91-57, 1991.
[15] Blazek J, Kroll N, Radespiel R, Rossow C-C. Upwind implicit residual smoothing method for multi-stage schemes. In: AIAA paper 91-1533. 1991.
[16] Blazek J. Computational fluid dynamics: Principles and applications. third ed.. Oxford: Butterworth-Heinemann; 2015, p. 283–335. http://dx.doi.org/10.1016/B978-0-08-099995-1.00009-9, Ch. 9 - Acceleration Techniques.
[17] Bassenne M, Fu L, Mani A. Time-accurate and highly-stable explicit operators for stiff differential equations. J Comput Phys 2021;424:109847. http://dx.doi.org/10.1016/j.jcp.2020.109847.
[18] Calvo M, Fu L, Montijano J, Rández L. Singly TASE operators for the numerical solution of stiff differential equations by explicit runge–kutta schemes. SIAM J Sci Comput 2023;96:17. http://dx.doi.org/10.1007/s10915-023-02232-3.
[19] Kennedy C, Gruber A. Reduced aliasing formulations of the convective terms within the Navier-Stokes equations. J Comput Phys 2008;227:1676–700.
[20] Coppola G, Capuanoa F, Pirozzoli S, de Luca L. Numerically stable formulations of convective terms for turbulent compressible flows. J Comput Phys 2019;382:86–104. http://dx.doi.org/10.1016/j.jcp.2019.01.007.
[21] Edoh A, Mundis N, Karagozian A, Sankaran V. Balancing aspects of numerical dissipation, dispersion, and aliasing in time-accurate simulations. Internat J Numer Methods Fluids 2020;92:1506–27. http://dx.doi.org/10.1002/fld.4837.
[22] Kuya Y, Kawai S. Modified wavenumber and aliasing errors of split convective forms for compressible flows. J Comput Phys 2022;464:111336. http://dx.doi.org/10.1016/j.jcp.2022.111336.
[23] Nagarajan S, Lele S, Ferziger J. A robust high-order compact method for large eddy simulation. J Comput Phys 2003;191:392–419.
[24] Gloerfelt X, Lafon P. Direct computation of the noise induced by a turbulent flow through a diaphragm in a duct at low mach number. Comput & Fluids 2008;37:388–401.
[25] Song H, Ghate A, Matsuno K, West J, Subramaniam A, Brown L, Lele S. Robust high-resolution simulations of compressible turbulent flows without filtering. In: AIAA paper 2022-4122. Chicago, Illinois: AIAA Aviation Forum; 2022, http://dx.doi.org/10.2514/6.2022-4122.
[26] Aubard G, Stefanin Volpiani P, Gloerfelt X, Robinet J-C. Comparison of subgrid-scale viscosity models and selective filtering strategy for large-eddy simulations. Flow Turbul Combust 2013;91(3):497–518.
[27] Gloerfelt X, Cinnella P. Large eddy simulation requirements for the flow over periodic hills. Flow Turbul Combust 2019;103(1):55–91.

[28] Lele S. Compact finite difference schemes with spectral-like resolution. J Comput Phys 1992;103:16–42.
[29] Gaitonde D, Visbal M. Padé-type higher-order boundary filters for the Navier-Stokes equations. AIAA J 2000;38(11):2103–12.
[30] Edoh A, Mundis N, Merkle C, Karagozian A, Sankaran V. Comparison of artificial-dissipation and solution-filtering stabilization schemes for time-accurate simulations. J Comput Phys 2018;375:1424–50. http://dx.doi.org/10.1016/j.jcp.2018.08.019.
[31] Kim J, Lee D. Adaptive nonlinear artifical dissipation model for computational aeroacoustics. AIAA J 2001;39(5):810–8.
[32] Yee H, Sandham N, Djomehri M. Low-dissipative high-order schock-capturing methods using characteristic-based filters. J Comput Phys 1999;150:199–238.
[33] Lamballais E, Vicente Cruz R, Perrin R. Viscous and hyperviscous filtering for direct and large-eddy simulation. J Comput Phys 2021;431:110115. http://dx.doi.org/10.1016/j.jcp.2021.110115.
[34] Jameson A, Schmidt W, Turkel E. Numerical solutions of the Euler equations by finite volume methods using Runge-Kutta time-stepping schemes. In: AIAA paper 81-1259. 1981.
[35] Wigton L, Swanson R. Variable coefficient implicit residual smoothing. In: Morton K, editor. Twelfth international conference on numerical methods in fluid dynamics, vol. 371 of lecture notes in physics. Berlin, Heidelberg: Springer; 1990, http://dx.doi.org/10.1007/3-540-53619-1_190.
[36] Ni M, Xi G, Wang S. Construction of high-order accuracy implicit residual smoothing schemes. Appl Math Mech 2000;21(4):407–14.
[37] Cinnella P, Lerat A. A fully implicit third-order scheme in time and space for compressible turbulent unsteady flow simulations. In: European congress on computational methods in applied sciences and engineering (ECCOMAS). Barcelona, Spain; 2000.
[38] Strikwerda J. Initial boundary value problems for the method of lines. J Comput Phys 1980;34:94–107.
[39] Couailler V, Liamis N. Unsteady Euler and Navier-Stokes flows simulations with an implicit Runge-Kutta method. In: Computational fluid dynamics'94. J. Wiley; 1994, p. 917–24.
[40] Gustafsson B. On the implementation of boundary conditions for the method of lines. BIT Numer Math 1998;38:293–314. http://dx.doi.org/10.1007/BF02512369.
[41] Gasparo M, Pieraccini S. Implicit residual smoothing in a parallel 2D Euler solver. Int J Comput Math 1999;72:313–24.
[42] Povitsky A, Morris P. A high-order compact method in space and time based on parallel implementation of the Thomas algorithm. J Comput Phys 2000;161:182–203.
[43] Choi J, Dongarra J. Scalapack: a scalable linear algebra library for distributed memory concurrent computers. In: Proceedings of the fourth symposiumon the frontiers of massively parallel computation X. 1992, p. 120–7.
[44] Polizzi E, Sameh A. SPIKE: A parallel environment for solving banded linear systems. Comput & Fluids 2007;36:113–20.
[45] Ki-Ha K, Ji-Hoon K, Xiaomin P, Jung-Il C. PaScaL TDMA: A library of parallel and scalable solvers for massive tridiagonal systems. Comput Phys Comm 2021;260:107722.
[46] Borel C, Roux F. Implicit multi-domain method for unsteady compressible inviscid fluid flows around 3D projectiles. In: Reinsch K, Schmidt W, Ecer A, Häuser J, Periaux J, editors. Conference on parallel computational fluid dynamics, 10-12 1991. Germany: Elsevier Science Publishers B.V. Stuttgart; 1992, p. 47–58.
[47] Lerat A, Wu Z-N. Stable conservative multidomain treatments for implicit Euler solvers. J Comput Phys 1996;123:45–64.
[48] Wu Z-N, Zou H. Grid overlapping for implicit parallel computation of compressible flows. J Comput Phys 2000;157:2–43.
[49] Visbal M, Gaitonde D. High-order-accurate methods for complex unsteady subsonic flows. AIAA J 1999;37(10):1231–9.
[50] Bienner A, Gloerfelt X, Cinnella P. Assessment of a high-order implicit residual smoothing time scheme for multiblock curvilinear meshes. In: Eleventh international conference on computational fluid dynamics (ICCFD11). Maui, USA; p. 2022.
[51] Thomas P, Lombard C. Geometric conservation law and its application to flow computations on moving grids. AIAA J 1979;17(10):1030–7. http://dx.doi.org/10.2514/3.61273.
[52] Deng X, Mao M, Tu G, Liu H, Zhang H. Geometric conservation law and applications to high-order finite difference schemes with stationary grids. J Comput Phys 2011;230(4):1100–15. http://dx.doi.org/10.1016/j.jcp.2010.10.028.
[53] Tam C, Dong Z. Radiation and outflow boundary conditions for direct computation of acoustic and flow disturbances in a nonuniform mean flow. J Comput Acous 1996;4(2):175–201.
[54] Pulliam T. Artificial dissipation models for the Euler equations. AIAA J 1986;24(12):1931–40.
[55] Choi H, Moin P. Effect of the computational time-step on numerical solutions of turbulent flow. J Comput Phys 1994;113:1–4.
[56] Vreman A, Kuerten J. Comparison of direct numerical simulation databases of turbulent channel flow at re_τ=180. Phys Fluids 2014;26:015102.
[57] Stryjek R, Vera J. PRSV: An improved peng-robinson equation of state for pure compounds and mixtures. Can J Chem Eng 1986;64(2):323–33. http://dx.doi.org/10.1002/cjce.5450640224.
[58] Chung T, Ajlan M, Lee L, Starling K. Generalized multiparameter correlation for nonpolar and polar fluid transport properties. Ind Eng Chem Res 1988;27(4):671–9.
[59] Gloerfelt X, Bienner A, Cinnella P. High-subsonic boundary-layer flows of an organic vapour. 971, 2023, p. A8. http://dx.doi.org/10.1017/jfm.2023.633,
[60] Schlatter P, Örlü R. Assessment of direct numerical simulation data of turbulent boundary layers. J Fluid Mech 2010;659:116–26.
[61] Bijl H, Carpenter M, Vatsa V, Kennedy C. Implicit time integration schemes for the unsteady compressible Navier-Stokes equations: Laminar flow. J Comput Phys 2002;179:313–29. http://dx.doi.org/10.1006/jcph.2002.7059.
[62] Grimich K, Michel B, Cinnella P, Lerat A. An accurate finite-volume formulation of a residual-based compact scheme for unsteady compressible flows. Comput & Fluids 2014;92:93–112. http://dx.doi.org/10.1016/j.compfluid.2013.12.016.
[63] Parnaudeau P, Carlier J, Heitz D, Lamballais E. Experimental and numerical studies of the flow over a circular cylinder at Reynolds number 3900. Phys Fluids 2008;20:085101.
[64] 4th International Workshop on High-Order CFD Methods, sponsored by NASA, AIAA, DLR and Army Research Office (ARO). In: June 3-4 2015 at the Eccomas / 6th European conference on CFD (ECFD VI), crete, case AS1. https://how4.cenaero.be/content/as1-dnsles-infinite-cylinder-re3900.
[65] Norberg C. Effects of reynolds number and low-intensity free stream turbulence on the flow around a circular cylinder. Tech. Rep. 87-2,, Gothenburg, Sweden: Chalmers University of Technology, Department of Applied Thermoscience and Fluid Mechanics; 1987.
[66] Lourenco LM, Shih C. Characteristics of the plane turbulent near wake of a circular cylinder, a particle image velocimetry study, published in Ref. [89], 1994.
[67] Thompson M, Hourigan K. The shear-layer instability of a circular cylinder wake. Phys Fluids 2005;17:021702.
[68] Lehmkuhl O, Rodríguez I, Borrell R, Oliva A. Low-frequency unsteadiness in the vortex formation region of a circular cylinder. Phys Fluids 2013;25:085109. http://dx.doi.org/10.1063/1.4818641.
[69] Tian G, Xiao Z. New insight on large-eddy simulation of flow past a circular cylinder at subcritical Reynolds number 3900. AIP Adv 2020;10:085321. http://dx.doi.org/10.1063/5.0012358.
[70] Johnson T, Patel V. Flow past a sphere up to a Reynolds number of 300. J Fluid Mech 1999;378:19–70. http://dx.doi.org/10.1017/S0022112098003206.
[71] Tomboulides A, Orszag S. Numerical investigation of transitional and weak turbulent flow past a sphere. J Fluid Mech 2000;416:45–73. http://dx.doi.org/10.1017/S0022112000008880.
[72] Nagata T, Nonomura T, Takahashi S, Mizuno Y, Fukuda K. Investigation on subsonic to supersonic flow around a sphere at low Reynolds number of between 50 and 300 by direct numerical simulation. Phys Fluids 2016;28:056101. http://dx.doi.org/10.1063/1.4947244.
[73] Sansica A, Ohmichi Y, Robinet J-C, Hashimoto A. Laminar supersonic sphere wake unstable bifurcations. Phys Fluids 2020;32:126107. http://dx.doi.org/10.1063/5.0031599.
[74] Taneda S. Experimental investigation of the wake behind a sphere at low Reynolds numbers. J Phys Soc Japan 1956;11(10):1104–8.
[75] Roos F, Willmarth W. Some experimental results on sphere and disk drag. AIAA J 1971;9(2):285–91. http://dx.doi.org/10.2514/3.6164.
[76] Cinnella P. Simulation d'écoulements compressibles turbulents autour de profils oscillants par une méthode numérique de haute précision. (Ph.D. thesis), Ecole Nationale Supérieure d'Arts et Métiers, no 1999-21; 1999.
[77] Leweke T, Provansal M, Ormières D, Lebescond R. Vortex dynamics in the wake of a sphere. Phys Fluids 1999;11:S12. http://dx.doi.org/10.1063/1.4739162.
[78] Sakamoto H, Haniu H. A study on vortex shedding from spheres in a uniform flow. ASME J Fluids Eng 1990;112(4):386–92. http://dx.doi.org/10.1115/1.2909415.
[79] Yun G, Kim D, Choi H. Vortical structures behind a sphere at subcritical Reynolds numbers. Phys Fluids 2006;5:015102. http://dx.doi.org/10.1063/1.2166454.
[80] Rodriguez I, Borrell R, Lehmkuhl O, Perez Segarra C, Oliva A. Direct numerical simulation of the flow over a sphere at Re=3700. J Fluid Mech 2011;679:263–87. http://dx.doi.org/10.1017/jfm.2011.136.
[81] Bazilevs Y, Yan J, de Stadler M, Sarkar S. Computation of the flow over a sphere at Re=3700: A comparison of uniform and turbulent inflow conditions. ASME J Appl Mech 2014;81(12):121003. http://dx.doi.org/10.1115/1.4028754.
[82] Li D, Luo K, Zhao H, Shang W, Fan J. Interaction between a stationary sphere and turbulent flow in a boundary layer. Phys Fluids 2022;34:085138. http://dx.doi.org/10.1063/5.0102429.
[83] Nagata T, Nonomura T, Takahashi S, Fukuda K. Direct numerical simulation of subsonic, transonic and supersonic flow over an isolated sphere up to a Reynolds number of 1000. J Fluid Mech 2020;904:A36. http://dx.doi.org/10.1017/jfm.2020.629.
[84] Kim H, Durbin P. Observations of the frequencies in a sphere wake and of drag increase by acoustic excitation. Phys Fluids 1988;31(11):3260–5. http://dx.doi.org/10.1063/1.866937.
[85] Schlichting H. Boundary layer theory. 6th Edition. McGraw-Hill; 1968.
[86] Saliba G. Study and development of fluidic micro-oscillators for cooling electronic systems. (Ph.D. thesis), Université Paul Sabatier-Toulouse III; 2022.

[87] Yalçın O, Saliba G, Gloerfelt X, Batikh A, Baldas L. Numerical investigation of a pulsed jet actuator having non-negligible switching time. AIAA J 2023;61(10):4345–55.

[88] Matar C, Cinnella P, Gloerfelt X. Numerical investigation of the transonic non-ideal gas flow around a circular cylinder at high Reynolds number. Flow Turbul Combust 2023. http://dx.doi.org/10.1007/s10494-023-00496-1.

[89] Beaudan P, Moin P. Numerical experiments on the flow past a circular cylinder at sub-critical reynolds number. In: CTR annual research briefs. NASA Ames/Stanford University; 1994.